<u>Gö-VIP-10:</u> **Dr. Francesca Odoardi / Prof. Dr. Alexander Flügel**
Institut für Neuroimmunologie, Institut für Multiple-Sklerose-Forschung

Autoren: **Schläger C**[1], **Körner H**[1], Krueger M[2], Vidoli S[3], **Haberl M**[1], Mielke D[4], Brylla E[2], Issekutz T[5], Cabañas C[6], Nelson PJ[7], Ziemssen T[8], Rohde V[4], Bechmann I[2], **Lodygin D**[1], **Odoardi F**[1], **Flügel A**[1,9] *.

[1]**Institute of Neuroimmunology, Institute for Multiple Sclerosis Research, University Medical Centre Göttingen, 37073 Göttingen, Germany.**

[2]Institute of Anatomy, University of Leipzig, 04103 Leipzig, Germany.

[3]Department of Structural and Geotechnical Engineering, University of Rome La Sapienza, 00185 Rome, Italy.

[4]Department Neurosurgery, University Medical Centre Göttingen, 37075 Göttingen, Germany.

[5]Division of Immunology, Department of Pediatrics Dalhousie University, Halifax B3H 4R2, Canada.

[6]Departamento de Biología Celular e Inmunología, Centro de Biología Molecular Severo Ochoa, 28049 Madrid, Spain.

[7]Medical Clinic and Policlinic IV, Ludwig-Maximilians-University of Munich, 80336 Munich, Germany.

[8]Department of Neurology, University Hospital, 01307 Dresden, Germany.

[9]Max-Planck-Institute for Experimental Medicine, 37075 Göttingen, Germany.

*Corresponding Author

Zusammenfassung des wissenschaftlichen Inhalts
(Prof. Dr. Alexander Flügel)

Das Zentralnervensystem (ZNS) ist vollständig von Flüssigkeit, dem Nervenwasser (Liquor cerebrospinalis, kurz Liquor) umgeben. Der Liquor wird mehrmals täglich komplett ausgetauscht, d.h. er wird ständig neu gebildet und an anderer Stelle absorbiert. Das bedingt, dass der Liquor, ähnlich wie das Blut oder die Lymphe, zirkuliert. Diese „dritte Zirkulation" (neben Blut und Lymphe) kann Stoffe oder Zellen zum Nervengewebe hin oder davon wegtransportieren. In dieser Arbeit befassten wir uns mit der Frage, wie Immunzellen, hier speziell autoaggressive T-Zellen in einem Modell für Multiple Sklerose (MS), in den Liquor gelangen, welche Funktion sie dort haben und ob/wie die Zellen zwischen dem Liquor und dem Nervengewebe kommunizieren. Mittels intravitaler Echtzeitmikroskopie konnten wir zeigen, dass die Hirnhaut, die direkt auf der Oberfläche des Nervengewebes liegt, eine entscheidende Schaltstelle für die Wanderung von T-Zellen darstellt. T-Zellen auf dem Weg in das ZNS verlassen die Blutbahn aus Gefäßen dieser Hirnhaut. Die Gefäße sind in der Hirnhaut eingebettet und von zahlreichen faserigen Bindegewebsstrukturen umschnürt. Der Liquor fließt über und durch dieses Faser-Zellgeflecht. Wir konnten beobachten, dass T-Zellen, die direkt an der Expositionsfläche zum Liquor entlangkriechen, in den Liquor geschwemmt werden. Dieses Abspülen der Zellen wurde durch Fresszellen, die in den

Hirnhäuten sitzen und den T-Zellen Signale für die Aktivierung und für die Anheftung liefern können, verhindert. T-Zellen suchten diese meningealen Fresszellen systematisch nach diesen Signalen ab. Blieben die Signale aus, liefen Zellen Gefahr, in den Liquor abgeschwemmt zu werden. Bekamen sie dagegen die nötigen Aktivierungs- oder Adhäsionssignale, hafteten sie an der Oberfläche fest und konnten in das Nervengewebe eindringen, wo sie, im Falle der Autoimmunerkrankung MS, den destruktiven Entzündungsprozess starteten. Außerdem stellte sich heraus, dass die T-Zellen im Liquor vollständig funktionstüchtig waren. Die T-Zellen konnten zwischen Liquor und dem angrenzenden Hirnhautgewebe hin- und herpendeln. Dieses Wiederandocken an die Hirnhautoberfläche ähnelte dem Anheftungsprozess der T-Zellen beim Austritt aus den Blutgefäßen in das Hirngewebe. Stabil kleben blieben die Zellen vor allem, wenn sie auf Fresszellen trafen, die besonders hohe Mengen an Adhäsionsfaktoren für die T-Zellen produzierten, was z.B. bei einer Entzündung des Hirngewebes der Fall ist, oder wenn die Fresszellen Aktivierungssignale für die T-Zellen lieferten.

Diese Ergebnisse geben neue Einblicke in die Immunfunktion des Liquors. Im Liquor landen vor allem T-Zellen, die vergeblich die Hirnhäute auf Anwesenheit ihres spezifischen Eiweißes oder von Entzündung abgesucht haben. Der Liquor stellt daher für T-Zellen eine Art Abstellkammer dar, die dafür sorgt, dass die potenziell gefährlichen Eindringlinge vom empfindlichen Nervengewebe ferngehalten werden. Allerdings können sich die zirkulierenden Zellen bei Bedarf jederzeit wieder an die Hirnhaut anheften und in das Nervengewebe eindringen. Eine genauere Aussage über die Zellen und deren Funktion im Liquor könnte daher sowohl diagnostisch als auch therapeutisch genutzt werden.

WEITERE INFORMATIONEN:

Prof. Dr. Alexander Flügel

Institut für Neuroimmunologie

Waldweg 33, 37073 Göttingen

E-Mail: fluegel@med.uni-goettingen.de

LETTER

Effector T-cell trafficking between the leptomeninges and the cerebrospinal fluid

Christian Schläger[1]*, Henrike Körner[1]*, Martin Krueger[3], Stefano Vidoli[4], Michael Haberl[1], Dorothee Mielke[5], Elke Brylla[3], Thomas Issekutz[6], Carlos Cabañas[7], Peter J. Nelson[8], Tjalf Ziemssen[9], Veit Rohde[5], Ingo Bechmann[3], Dmitri Lodygin[1], Francesca Odoardi[1]* & Alexander Flügel[1,2]*

In multiple sclerosis, brain-reactive T cells invade the central nervous system (CNS) and induce a self-destructive inflammatory process. T-cell infiltrates are not only found within the parenchyma and the meninges, but also in the cerebrospinal fluid (CSF) that bathes the entire CNS tissue[1,2]. How the T cells reach the CSF, their functionality, and whether they traffic between the CSF and other CNS compartments remains hypothetical[3–6]. Here we show that effector T cells enter the CSF from the leptomeninges during Lewis rat experimental autoimmune encephalomyelitis (EAE), a model of multiple sclerosis. While moving through the three-dimensional leptomeningeal network of collagen fibres in a random Brownian walk, T cells were flushed from the surface by the flow of the CSF. The detached cells displayed significantly lower activation levels compared to T cells from the leptomeninges and CNS parenchyma. However, they did not represent a specialized non-pathogenic cellular sub-fraction, as their gene expression profile strongly resembled that of tissue-derived T cells and they fully retained their encephalitogenic potential. T-cell detachment from the leptomeninges was counteracted by integrins VLA-4 and LFA-1 binding to their respective ligands produced by resident macrophages. Chemokine signalling via CCR5/CXCR3 and antigenic stimulation of T cells in contact with the leptomeningeal macrophages enforced their adhesiveness. T cells floating in the CSF were able to reattach to the leptomeninges through steps reminiscent of vascular adhesion in CNS blood vessels, and invade the parenchyma. The molecular/cellular conditions for T-cell reattachment were the same as the requirements for detachment from the leptomeningeal milieu. Our data indicate that the leptomeninges represent a checkpoint at which activated T cells are licensed to enter the CNS parenchyma and non-activated T cells are preferentially released into the CSF, from where they can reach areas of antigen availability and tissue damage.

T cells specific for myelin basic protein (MBP) retrovirally transduced to express fluorescent proteins (T_{MBP} cells) were tracked on their way into the CNS tissues after intravenous (i.v.) transfer to healthy recipient rats. The T_{MBP} cells arrived at the CNS on the level of the leptomeninges of the spinal cord before they entered the parenchyma with the onset of clinical disease[7]. Concomitantly to their arrival in the leptomeningeal milieu, T_{MBP} cells accumulated in the CSF (Extended Data Fig. 1a, b).

It has been proposed that immune cells, for example, T helper 17 (T_H17) cells and M2 macrophages, enter the CSF from either the leptomeninges or the choroid plexus before spreading to the CNS tissues[3–6,8,9]. We could not detect T_{MBP} cells in the choroid vessels or stroma before or during their accumulation in the CSF when we used

intravital two-photon laser scanning microscopy (TPLSM) to image the choroid plexus of the fourth ventricle. Very few cells appeared in the choroid plexus at late phases of CNS infiltration, when T_{MBP} cells had already maximally accumulated in the leptomeninges and CSF (Fig. 1a). Serial fluorescence microscopy of all four choroid plexus, immuno-electron microscopy and cytofluorometric quantifications revealed similar results (Extended Data Fig. 1c–f). To exclude the possibility of transport of T_{MBP} cells from the choroid plexus to the leptomeninges of the spinal cord, we injected a nontoxic polymerizing agent (Matrigel) into the cisterna magna, that is, between the ventricular egression points and subarachnoidal space of the spinal cord[8]. The cisternal block neither prevented the invasion of T_{MBP} cells into the subjacent spinal cord nor influenced the development of clinical disease (Extended Data Fig. 2a, b). Similarly, interrupting the CSF flow from the choroid plexus to the spinal cord did not hinder the accumulation of T_{MBP} cells in the lumbar/thoracic spinal cord (Extended Data Fig. 2c–e).

T_{MBP} cells crawling within the leptomeningeal vessels transgressed the vascular walls (Extended Data Fig. 3a) and moved within the leptomeningeal environment (Supplementary Video 1). This milieu is highly specialized: the pial vessels that run along the surface of the spinal cord parenchyma are suspended in a dense three-dimensional (3D) extracellular matrix (ECM) network consisting mainly of collagen fibrils[7] (Extended Data Fig. 3b). Just as the bloodstream flows over the vascular endothelia, the CSF within the subarachnoidal space flows over the pial ECM network. Interestingly, when following the movement of single migrating T_{MBP} cells, we regularly observed them at the interface of the ECM network and fluidic compartment becoming detached and being washed into the CSF (Fig. 1b, Extended Data Fig. 3c, Supplementary Videos 2 and 3). This detachment was verified by imaging *in situ* labelled T cells expressing the photo-convertible fluorescent protein Dendra2 (Extended Data Fig. 3d, e, Supplementary Video 4). Photo-converted $T_{MBP–Dendra2}$ cells in the leptomeninges steadily decreased over time and were replaced by non-photo-converted $T_{MBP–Dendra2}$ cells, indicating rapid turnover of T cells in this CNS compartment (Extended Data Fig. 3e).

RNA sequencing (RNA-seq) revealed that T_{MBP} cells from the blood, CSF, leptomeninges and spinal cord parenchyma displayed broad conformity of their gene expression profiles, with very similar expression levels of master transcription factors, chemokine receptors, adhesion molecules, cytokine receptors, cell motility and T-cell receptor genes (Fig. 2a, Extended Data Fig. 4a, b, Supplementary Table 1). The exceptions were genes of the T-cell activation program: T_{MBP} cells from the leptomeninges and CNS parenchyma displayed strongly upregulated genes of cytokine–cytokine-receptor interaction,

[1]Institute of Neuroimmunology, Institute for Multiple Sclerosis Research, University Medical Centre Göttingen, 37073 Göttingen, Germany. [2]Max-Planck-Institute for Experimental Medicine, 37075 Göttingen, Germany. [3]Institute of Anatomy, University of Leipzig, 04103 Leipzig, Germany. [4]Department of Structural and Geotechnical Engineering, University of Rome La Sapienza, 00185 Rome, Italy. [5]Department Neurosurgery, University Medical Centre Göttingen, 37075 Göttingen, Germany. [6]Division of Immunology, Department of Pediatrics Dalhousie University, Halifax B3H 4R2, Canada. [7]Departamento de Biología Celular e Inmunología, Centro de Biología Molecular Severo Ochoa, 28049 Madrid, Spain. [8]Medical Clinic and Policlinic IV, Ludwig-Maximilians-University of Munich, 80336 Munich, Germany. [9]Department of Neurology, University Hospital, 01307 Dresden, Germany.
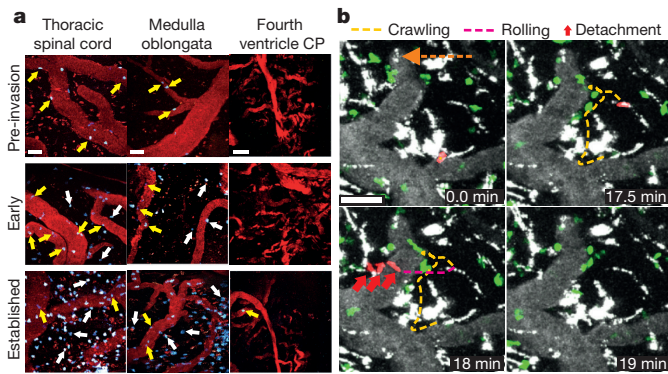*These authors contributed equally to this work.

Figure 1 | T_{MBP} cells enter the CSF from the leptomeninges. a, Intravital imaging of T_{MBP} cell entry into the leptomeninges and choroid plexus (CP) of the fourth ventricle. TPLSM recordings were performed during the pre-invasion, early and established phases of leptomeningeal T-cell infiltration (see Methods for the definition of phases) sequentially in thoracic spinal cord, medulla and choroid plexus of fourth ventricle in the same animal. Representative recordings of 16 independent experiments. Blue, $T_{MBP–Lifeact–Turquoise2}$ cells; red, vessel lumen, meningeal macrophages; yellow and white arrows, intravascular and extravasated cells, respectively. **b**, *In vivo* visualization of T_{MBP} cell detachment from the leptomeninges into the CSF. Intravital images of leptomeninges during the established phase of leptomeningeal T-cell infiltration showing a $T_{MBP–GFP}$ cell (false red colour) detaching from the pial surface. Yellow lines, crawling steps of a $T_{MBP–GFP}$ cell; magenta line, migratory path of a T cell rolling on the leptomeninges and being dragged away into the CSF; grey (false colour), vessel lumen, meningeal macrophages; red arrows, $T_{MBP–GFP}$ cell detachment; orange arrow, CSF flow direction. Scale bars, 50 μm.

JAK–STAT signalling and T-cell receptor signalling pathways, whereas CSF-derived T_{MBP} cells resembled blood-derived T cells that lacked virtually any signs of activation (Fig. 2b, Extended Data Fig. 4b–e, Supplementary Tables 2 and 3). TPLSM recording of the nuclear translocation of a fluorescently labelled nuclear factor of activated T cells (NFAT–YFP) sensor[10] confirmed these findings: in contrast to the leptomeninges and the CNS parenchyma where 26% and 35%, respectively, of the $T_{MBP–NFAT/YFP}$ cells showed nuclear translocations of the sensor, virtually no $T_{MBP–NFAT/YFP}$ cells in the CSF displayed nuclear NFAT translocations (< 2%; Fig. 2c).

The low activation profile of CSF-derived T_{MBP} cells could not be explained by inhibitory effects of the CSF on T-cell activation (Extended Data Fig. 4f). Most notably, CSF-derived T_{MBP} cells were fully responsive to antigenic stimulation and induced 'classic' EAE (Fig. 2d), indicating that T cells in the CSF—despite their reduced activation levels—were fully functional.

We next performed i.v. transfer of myelin oligodendrocyte glycoprotein (MOG)-reactive T cells (T_{MOG} cells), which enter the CNS tissues but reach only low reactivation levels within the CNS and induce very mild clinical disease[11] (Extended Data Fig. 5a). T_{MOG} cells invaded the CNS parenchyma to a lesser extent than T_{MBP} cells but remained in higher percentages in the CSF and leptomeninges (Fig. 2e and Extended Data Fig. 5b). This shifted distribution pattern became even more pronounced when brain non-reactive ovalbumin-specific T cells (T_{OVA} cells) were transferred into rats. They entered in the CNS milieu similarly to T_{MBP} or T_{MOG} cells, though in much lower numbers (Fig. 2e), but mostly remained in the CSF/leptomeninges compartments (Fig. 2e and Extended Data Fig. 5b) and did not evoke any detectable CNS inflammation (Extended Data Fig. 5c).

The situation markedly changed in inflamed CNS tissue. When T_{OVA} cells were co-transferred with pathogenic T_{MBP} cells that induced a strong upregulation of chemokines, integrin ligands and cytokines within the leptomeninges and parenchyma, high numbers of T_{OVA} cells, irrespective of their low activation levels, invaded the CNS and migrated from the CSF/leptomeninges compartments deep into the

CNS parenchyma (Fig. 2e and Extended Data Fig. 5b–d). There were still more T_{OVA} cells in the CSF than T_{MBP} cells, indicating that even during CNS inflammation the lack of T-cell reactivation affects the adhesiveness of T_{OVA} cells within the leptomeningeal milieu (Extended Data Fig. 5e). Taken together, these data indicate that in addition to the T-cell reactivation state, inflamed CNS tissue supports T-cell attachment to the leptomeninges and migration into the CNS parenchyma.

We next investigated the cellular partners and molecular cues that guide T cells within the leptomeningeal milieu. Enmeshed in the pial ECM are numerous macrophages that scan their environment by protruding and retracting cellular processes (Extended Data Fig. 6a). T_{MBP} cells crawling through the leptomeningeal milieu were in contact with these cells the majority of the time (> 70%) (Extended Data Fig. 6a, b, Supplementary Video 5). In contrast to T cells in lymphatic tissue[12], the T_{MBP} cells in the leptomeninges moved in a Brownian random walk (Fig. 3a, b) not following measurable microgradients (Extended Data Fig. 6c). CD8^{+} T cells searching for rare infectious foci during toxoplasma infection of the CNS displayed a Lévy walk behaviour that is characterized by a combination of random walk and large jumps[13]. Apparently when the interacting partners within the CNS tissue are abundant, as is the case with leptomeningeal macrophages, Brownian motion is sufficiently efficient[14]. Meningeal macrophages express major histocompatibility complex (MHC) class II molecules on their surface and therefore can act as antigen-presenting cells[10,15,16]. In addition, they express fibronectin and ICAM-1 (Extended Data Fig. 6d), that is, ligands of VLA-4 (α4β1) and LFA-1 (αLβ2) integrins expressed by T_{MBP} cells (Extended Data Fig. 7a). *In situ* staining with an antibody directed against the activated conformation of VLA-4 revealed that 10% of the T_{MBP} cells within the leptomeninges, but none in the CSF, carried activated integrin on their membrane (Extended Data Fig. 7b). Intrathecal (i.t.) injection of neutralizing anti-VLA-4 and/or anti-LFA-1 monoclonal antibodies shortened the contact time of T_{MBP} cells with leptomeningeal phagocytes, whereas the contact frequency increased (Fig. 3c). Furthermore, in the presence of the CSF flow, the velocity of the T cells increased (Fig. 3c, Extended Data Fig. 7c, d), but their random walk behaviour remained unaffected (Extended Data Fig. 7e). Interestingly, we noted a large leptomeningeal detachment of T_{MBP} cells that then rolled along the pial surface or floated in the CSF (Fig. 3d, e, Extended Data Fig. 7f, Supplementary Video 6). Accordingly, photo-converted $T_{MBP–Dendra2}$ cells vanished more rapidly from the leptomeninges after VLA-4/LFA-1 interference (Extended Data Fig. 7g).

Chemokines are known to activate the integrin-mediated binding of immune cells[17]. T_{MBP} cells upregulate chemokine receptors before entering the CNS, in particular CCR5, CXCR3 and CXCR4 (ref. 18; Extended Data Fig. 8a). The corresponding chemokines (CCL5, CXCL9–11 and CXCL12) were present in the CNS tissues and specifically expressed by the resident macrophages (Extended Data Fig. 8b–d). After i.t. application of pertussis toxin (PTX; which acts as a global chemokine inhibitor), high numbers of T_{MBP} cells became detached from the pial surface and were dragged into the CSF (Extended Data Fig. 8e, Supplementary Video 7). Their random walk behaviour and straightness of movement were unchanged but their contact time with the resident macrophages decreased (Extended Data Fig. 8f, g). In contrast to integrin blockade, the T-cell velocity remained unchanged (Extended Data Fig. 8f). Similar observations were made after i.t. injection of Met-RANTES and anti-CXCR3 monoclonal antibodies, which specifically interfere with CCR5 and CXCR3, respectively. In contrast, the CXCR4 blocker AMD3100 had no effect (Fig. 3f, Extended Data Fig. 8f, h).

T_{OVA} cells also migrated in a Brownian locomotion pattern and came into contact with the local macrophages, but these contacts were less frequent and shorter than those of T_{MBP} cells and their velocity was higher (Extended Data Fig. 9a–c). Interfering with integrins or chemokines also caused a strong detachment of T_{OVA} cells from the leptomeninges (Extended Data Fig. 9d, e). Notably, neither integrin
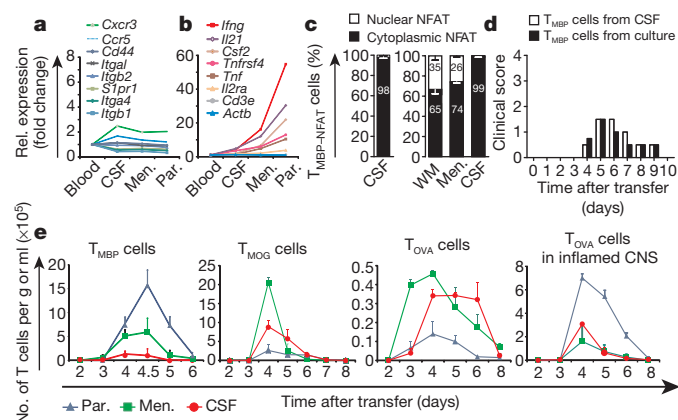
Figure 2 | Characterization of T_{MBP} cells in the CSF. a, Similarities in transcriptome profiles between T_{MBP} cells in blood, CSF, leptomeninges and CNS parenchyma. RNA-seq was performed for $T_{MBP–GFP}$ cells sorted from the indicated compartments 3 days after transfer, and relative (rel.) mRNA expression of selected adhesion molecules and chemokine receptor genes is shown. **b**, Genes related to T-cell activation are upregulated in T_{MBP} cells from meninges and CNS parenchyma compared to CSF. Relative mRNA expression (RNA-seq analyses) of selected genes that are highly regulated in $T_{MBP–GFP}$ cells from the indicated CNS compartments. Expression levels in the T cells isolated from blood was set to 1 (**a**, **b**). House-keeping genes, *Actb* and *Cd3e*. **c**, *In vivo* analyses of $T_{MBP–NFAT}$ cells confirm that their activation levels within the leptomeninges exceed those in the CSF. Percentages of cells with either cytoplasmic (not activated) or nuclear (activated) NFAT sensor during the established phase of leptomeningeal T-cell infiltration were determined by TPLSM (218 cells from 5 independent experiments, left plot) or by histology of SC cryosections (white matter (WM): 352 cells, meninges: 1,371 cells) and of cytospin preparations (CSF: 326 cells), right plot. Data are mean ± s.d. **d**, T_{MBP} cells in the CSF retain their pathogenic potential. 1.7×10^6 *in vitro* reactivated $T_{MBP–GFP}$ cells isolated from CSF of animals 3 days after transfer or an equivalent number of *in vitro* T cell blasts were injected i.v. into naive animals. Representative clinical score of 2 independent experiments ($n = 6$). The moderate severity of clinical disease is due to the low amount of injected T cells. **e**, T-cell reactivation and inflammatory state of the CNS tissue determine T-cell trafficking from leptomeninges into the CSF or CNS parenchyma. Flow cytometry quantification of antigen-specific T cells in the CNS compartments at the indicated time points after transfer. The first three plots show $T_{MBP–GFP}$ cells, $T_{MOG–GFP}$ cells and $T_{OVA–GFP}$ cells with high, low or no reactivation potential, respectively. Right, $T_{OVA–GFP}$ cell distribution in an inflamed CNS tissue (co-transfer with non-labelled T_{MBP} cells). Data are mean ± s.e.m. of at least 6 animals per group per time point for each antigen specificity from at least 2 independent experiments.
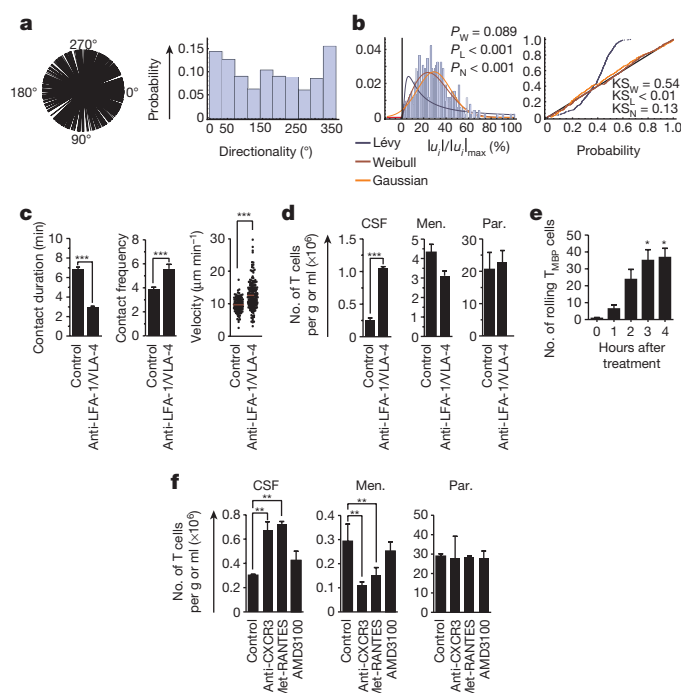

Figure 3 | Integrins and chemokines mediate T_{MBP} cell adhesion to leptomeningeal structures. a, **b**, TPLSM recordings show the motility behaviour of $T_{MBP–GFP}$ cells in the leptomeningeal milieu. Time interval, 32 s. **a**, T_{MBP} cells do not follow a preferential direction. Directions (left) and associated probability for 0–360° angles (right). **b**, T_{MBP} cells move in a Brownian random walk. Left, probability distribution of T-cell displacements in a linear scale with overlapping fitting of the displacement norm ($|\mathbf{u}_i|$) for Lévy (blue), Weibull (brown) and normal (Gaussian, orange) distributions. Respective P values are indicated. Only the Weibull distribution (equivalent to Brownian movement) has statistical significance. Right, probability plots of the indicated distributions against the displacement norm data with the associated results of Kolmogorov–Smirnov (KS) test. Analysis of at least 9 TPLSM recordings. **c**, Integrin blockade interferes with T cell and antigen-presenting cell contact and accelerates T-cell migration. Intravital 30 min TPLSM recordings. Mean contact duration (529 contacts per 208 cells), contact frequency (208 cells) between $T_{MBP–GFP}$ cells and leptomeningeal phagocytes and velocity (320 cells) before (control) and 4 h after i.t. injection of LFA-1/VLA-4-blocking monoclonal antibodies. **d**, **e**, Integrin blockade induces a release of T_{MBP} cells from the meninges into the CSF and increases T-cell rolling. **d**, Flow cytometry quantification of $T_{MBP–GFP}$ cells in the different CNS compartments 4 h after i.t. treatment with PBS (control) or blocking antibodies. Data are mean ± s.e.m. of 3 independent experiments (**c**, **d**) including three animals per group (**d**) (two-tailed Mann–Whitney U-test). **e**, Number of $T_{MBP–GFP}$ cells rolling on the pial surface during 10 min TPLSM recordings before (0 h) and at the indicated time points after integrin blockade. **f**, Interference with chemokine signalling induces a release of T_{MBP} cells from the leptomeninges into the CSF. Flow cytometry quantification of $T_{MBP–GFP}$ cells in the different CNS compartments 4 h after i.t. treatment with PBS (control), anti-CXCR3 monoclonal antibody, Met-RANTES or AMD3100. Data are mean ± s.e.m. of representative data from two (**e**) or three (**f**) independent experiments including three animals per group (Kruskal–Wallis ANOVA followed by Dunn's multiple comparison test). Analyses performed during the established phase of leptomeningeal T_{MBP} cell infiltration (**a**–**f**). *$P < 0.05$, **$P < 0.01$, ***$P < 0.001$ (**c**–**f**).

nor chemokine interference influenced the basal locomotion characteristics or the Brownian motility pattern of T_{OVA} or T_{MBP} cells (Extended Data Figs 8f, g, and 9f–h). These findings indicate that effector T cells in the 3D network of the leptomeninges—similarly to dendritic cells in a 3D environment[19]—are integrin-independent and follow an intrinsic locomotion program independent of chemokinetic or chemoattractive stimuli. In contrast, the interactions with local antigen-presenting cells are regulated by chemokine- and integrin-mediated adhesive forces that prevent effector T cells from being released into the CSF from the flow-exposed 2D milieu of the leptomeninges.

T cells were previously proposed to migrate from the CNS tissues via the CSF along lymphatic vessels of the dura mater[20,21], but it is unclear whether T cells in the CSF also return to the leptomeninges and the CNS parenchyma. After i.t. injection, T_{MBP} cells were indeed spread within the leptomeninges and the adjacent parenchyma (Extended Data Fig. 10a). This infiltration pattern resembled that of early EAE lesions but clearly differed from that of solutes[22], which were proposed to be transported from the CSF into the CNS parenchyma via peristaltic forces along periarterial spaces. This 'glymphatic' transport

mechanism does not seem to apply to cellular components[23]. We detected that T-cell transport in the CSF was mainly driven by the animal's respiration rather than the cardiac cycle[24] (Extended Data Fig. 10b, Supplementary Video 8). After injection of T_{MBP} cells into the subarachnoidal space of the cisterna magna or the lumbar spinal cord, the majority of cells accumulated at the levels of cell injections, that is, at the medulla/cervical and lumbar/thoracic spinal cord, respectively
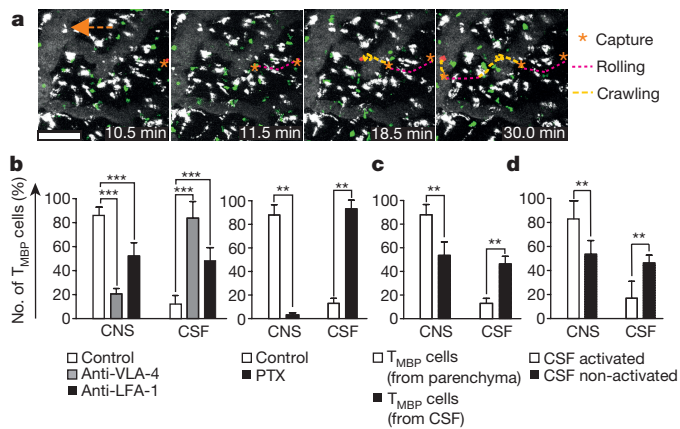
Figure 4 | Reattachment of effector T cells from the CSF to the leptomeninges and entry into the CNS parenchyma. a, *In vivo* visualization of T_{MBP} cell reattachment from the CSF to the leptomeninges. TPLSM recordings (30 min) during the established phase of leptomeningeal T_{MBP} cell infiltration. Example of a $T_{MBP-GFP}$ cell (false red colour) reattaching from the CSF to the pial surface with subsequent rolling (magenta dotted lines), capture (orange asterisks) and crawling steps (yellow dotted lines). Green, $T_{MBP-GFP}$ cells; grey (false colour), vessel lumen, meningeal macrophages; orange arrow, direction of CSF flow. Time interval, 32 s. Scale bar, 50 μm. **b–d,** Conditions that regulate T_{MBP} cell reattachment and entry into the CNS tissue. **b,** Blocking of integrin or $G\alpha_i$ signalling strongly reduces the capacity of T_{MBP} cells to migrate from the CSF into the CNS parenchyma. $T_{MBP-GFP}$ cells isolated from the CNS parenchyma were pre-treated with anti-VLA-4 or anti-LFA-1 monoclonal antibodies or with isotype control IgG (control) (left), or PTX or PBS (control) (right). The cells were then injected i.t. into naive animals. Entry of the transferred $T_{MBP-GFP}$ cells into the spinal cord (including meninges and parenchyma) and the CSF was quantified by flow cytometry 42 h later, that is, when the re-transferred T cells had maximally infiltrated the spinal cord of the recipient animals. Mean ± s.d. of representative results of 3 independent experiments ($n = 18$, Kruskal–Wallis ANOVA followed by Dunn's multiple comparison test (left) or two-tailed Mann–Whitney U-test, right). **c, d,** Activation fosters trafficking of T_{MBP} cells from the CSF into the CNS tissue. **c,** $T_{MBP-GFP}$ cells isolated from CSF or CNS parenchyma were injected i.t. into naive animals ($n = 6$). **d,** CSF-derived $T_{MBP-GFP}$ cells with or without previous antigenic stimulation *in vitro* were transferred i.t. Cell quantifications as in **b**. Data are mean ± s.d. of three (**c**) and two (**d**) independent experiments for each condition ($n = 8$, two-tailed Mann–Whitney U-test). **$P < 0.01$, ***$P < 0.001$ (**b–d**).

(Extended Data Fig. 10c). However, a considerable number of cells also reached remote areas of the CNS, indicating that the CSF can serve as transport medium for the cells. These distributions clearly differ from that of regular EAE (Extended Data Fig. 10d), in agreement with our observation that during EAE effector T cells enter the meningeal milieu via local vessels.

T_{MBP} cells initially floating within the CSF rolled along the pial surface and then stopped; thereafter, they continued their locomotion by crawling or rolling along the leptomeningeal structures (Fig. 4a, Supplementary Videos 4, 9 and 10), reminiscent of vascular adhesion steps[7,25]. The molecular requirements for the attachment of the T cells were also similar and included integrins and chemokines (Fig. 4b). However, the molecular range in leptomeningeal adhesion included LFA-1 in addition to VLA-4 (Fig. 4b), only the latter being a requirement for T-cell adhesion to the CNS endothelium[7]. Furthermore, integrin blockage completely abolished T-cell rolling along the endothelium[18], but not along the pial surface (Fig. 3e, Supplementary Video 6), indicating that during the leptomeningeal reattachment integrins control fixed adhesion of the T cells rather than their first initial binding steps. Another notable difference to vascular adhesion was the role of T-cell activation. CNS endothelial cells do not act as antigen-presenting cells for the incoming T_{MBP} cells[10]. However, antigen-driven T-cell activation significantly contributed to the T-cell reattachment in

the leptomeninges: non-activated CSF-derived $T_{MBP-GFP}$ cells entered the CNS tissue after i.t. injection less efficiently than their activated counterparts from the CNS parenchyma (Fig. 4c). When the CSF-derived T cells were activated before transfer, their invasive capacity significantly increased (Fig. 4d). Consequently, i.t.-transferred activated T_{MBP} cells invaded the CNS parenchyma and induced clinical EAE, whereas the resting cells were non-pathogenic (Extended Data Fig. 10e). Pretreatment of the activated T cells with anti-integrin monoclonal antibodies significantly reduced the severity of clinical EAE (Extended Data Fig. 10f). T_{OVA} cells attached less efficiently than T_{MBP} cells. However, when the T_{OVA} cells were activated, after antigenic stimulation before i.t. transfer or by evoking antigen-specific reactivation within the CNS by supplying OVA i.t.[26], they invaded the CNS more efficiently (Extended Data Fig. 10g).

The reattachment to the leptomeninges was not only dependent on the activation state of the T cells but also on the inflammatory state of the CNS tissue, as after i.t. transfer, T_{MBP} cells preferentially invaded inflamed CNS tissue compared to that of control rats (Extended Data Fig. 10h). The enhanced invasion could be substantially reverted by pretreating the cells with integrin/chemokine blockers before i.t. transfer (Extended Data Fig. 10i). Both observations indicate that the molecular/cellular requirements for reattachment of T cells from the CSF to the leptomeningeal milieu were the same as for their adhesion.

It is important to note that our findings were not an artefact of transfer EAE. In animals with active EAE induced by reactivated memory T_{MBP} cells[27], T cells exhibited a very similar trafficking behaviour and function in the CSF (Extended Data Fig. 10j–l).

Our data support the view that the leptomeninges represent an important checkpoint for T-cell infiltration of the CNS during autoimmune inflammation or immune surveillance[7,16,28]. Trafficking between CSF and CNS tissue is well regulated by integrin adhesive forces that are triggered by T-cell activation and/or chemokines[17,29] (Extended Data Fig. 10m), indicating that the CSF fulfils a dual role: it functions as a depot that prevents potentially dangerous effector T cells from entering the CNS parenchyma if these cells had unsuccessfully scanned the meninges for antigens or damage; and the circulating CSF can be used by T cells for residence or as transport medium, similar to blood circulation, to rapidly travel to damaged areas of the CNS. T cells in the CSF displayed very similar expression profiles to effector T cells that had invaded the CNS tissue. Furthermore, they maintained full antigen responsiveness and pathogenic potential. Therefore, the characterization of readily accessible T cells in the CSF could be of relevance for gaining insights into the properties and function of pathogenic T cells in multiple sclerosis.

1. Alvermann, S., Hennig, C., Stuve, O., Wiendl, H. & Stangel, M. Immunophenotyping of cerebrospinal fluid cells in multiple sclerosis: in search of biomarkers. *JAMA Neurol.* **71,** 905–912 (2014).
2. Giunti, D. *et al.* Phenotypic and functional analysis of T cells homing into the CSF of subjects with inflammatory diseases of the CNS. *J. Leukoc. Biol.* **73,** 584–590 (2003).
3. Kivisäkk, P. *et al.* Human cerebrospinal fluid central memory CD4+T cells: evidence for trafficking through choroid plexus and meninges via P-selectin. *Proc. Natl Acad. Sci. USA* **100,** 8389–8394 (2003).
4. Reboldi, A. *et al.* C-C chemokine receptor 6–regulated entry of T_H-17 cells into the CNS through the choroid plexus is required for the initiation of EAE. *Nature Immunol.* **10,** 514–523 (2009).
5. Engelhardt, B. & Ransohoff, R. M. The ins and outs of T-lymphocyte trafficking to the CNS: anatomical sites and molecular mechanisms. *Trends Immunol.* **26,** 485–495 (2005).
6. Engelhardt, B., Wolburg-Buchholz, K. & Wolburg, H. Involvement of the choroid plexus in central nervous system inflammation. *Microsc. Res. Tech.* **52,** 112–129 (2001).
7. Bartholomäus, I. *et al.* Effector T cell interactions with meningeal vascular structures in nascent autoimmune CNS lesions. *Nature* **462,** 94–98 (2009).

8. Shechter, R. *et al.* Recruitment of beneficial M2 macrophages to injured spinal cord is orchestrated by remote brain choroid plexus. *Immunity* **38,** 555–569 (2013).
9. Baruch, K. & Schwartz, M. CNS-specific T cells shape brain function via the choroid plexus. *Brain Behav. Immun.* **34,** 11–16 (2013).
10. Lodygin, D. *et al.* A combination of fluorescent NFAT and H2B sensors uncovers dynamics of T cell activation in real time during CNS autoimmunity. *Nature Med.* **19,** 784–790 (2013).
11. Kawakami, N. *et al.* The activation status of neuroantigen-specific T cells in the target organ determines the clinical outcome of autoimmune encephalomyelitis. *J. Exp. Med.* **199,** 185–197 (2004).
12. Castellino, F. *et al.* Chemokines enhance immunity by guiding naive CD8^{+} T cells to sites of CD4^{+} T cell–dendritic cell interaction. *Nature* **440,** 890–895 (2006).
13. Harris, T. H. *et al.* Generalized Lévy walks and the role of chemokines in migration of effector CD8^{+} T cells. *Nature* **486,** 545–548 (2012).
14. Humphries, N. E. *et al.* Environmental context explains Lévy and Brownian movement patterns of marine predators. *Nature* **465,** 1066–1069 (2010).
15. Mues, M. *et al.* Real-time *in vivo* analysis of T cell activation in the central nervous system using a genetically encoded calcium indicator. *Nature Med.* **19,** 778–783 (2013).
16. Kivisäkk, P. *et al.* Localizing central nervous system immune surveillance: meningeal antigen-presenting cells activate T cells during experimental autoimmune encephalomyelitis. *Ann. Neurol.* **65,** 457–469 (2009).
17. Laudanna, C., Kim, J. Y., Constantin, G. & Butcher, E. Rapid leukocyte integrin activation by chemokines. *Immunol. Rev.* **186,** 37–46 (2002).
18. Odoardi, F. *et al.* T cells become licensed in the lung to enter the central nervous system. *Nature* **488,** 675–679 (2012).
19. Lämmermann, T. *et al.* Rapid leukocyte migration by integrin-independent flowing and squeezing. *Nature* **453,** 51–55 (2008).
20. Louveau, A. *et al.* Structural and functional features of central nervous system lymphatic vessels. *Nature* **523,** 337–341 (2015).
21. Aspelund, A. *et al.* A dural lymphatic vascular system that drains brain interstitial fluid and macromolecules. *J. Exp. Med.* **212,** 991–999 (2015).
22. Iliff, J. J. *et al.* A paravascular pathway facilitates CSF flow through the brain parenchyma and the clearance of interstitial solutes, including amyloid β. *Sci. Transl. Med.* **4,** 147ra111 (2012).
23. Hatterer, E., Touret, M., Belin, M. F., Honnorat, J. & Nataf, S. Cerebrospinal fluid dendritic cells infiltrate the brain parenchyma and target the cervical lymph nodes under neuroinflammatory conditions. *PLoS ONE* **3,** e3321 (2008).
24. Dreha-Kulaczewski, S. *et al.* Inspiration is the major regulator of human CSF flow. *J. Neurosci.* **35,** 2485–2491 (2015).
25. Ley, K., Laudanna, C., Cybulsky, M. I. & Nourshargh, S. Getting to the site of inflammation: the leukocyte adhesion cascade updated. *Nature Rev. Immunol.* **7,** 678–689 (2007).
26. Odoardi, F., Kawakami, N., Klinkert, W. E., Wekerle, H. & Flügel, A. Blood-borne soluble protein antigen intensifies T cell activation in autoimmune CNS lesions and exacerbates clinical disease. *Proc. Natl Acad. Sci. USA* **104,** 18625–18630 (2007).
27. Kawakami, N. *et al.* Autoimmune CD4^{+} T cell memory: lifelong persistence of encephalitogenic T cell clones in healthy immune repertoires. *J. Immunol.* **175,** 69–81 (2005).
28. Lucchinetti, C. F. *et al.* Inflammatory cortical demyelination in early multiple sclerosis. *N. Engl. J. Med.* **365,** 2188–2197 (2011).
29. Dustin, M. L. & Springer, T. A. T-cell receptor cross-linking transiently stimulates adhesiveness through LFA-1. *Nature* **341,** 619–624 (1989).

Supplementary Information is available in the online version of the paper.

Author Contributions C.S. performed most intravital TPLSM imaging studies. H.K. performed most of the CSF analyses, fluorescence microscopy and T-cell-CSF-transfers. M.K., E.B. and I.B. performed and analysed immunofluorescence and electron microscopic analyses. S.V. performed the mathematical cell motility analyses. M.H. performed antibody labelling and contributed to TPLSM imaging. D.M. and V.R. designed the operative strategy, D.M. performed the plexus preparation. C.C. provided HUTS4 antibody and contributed with technical advice. T.I. provided the anti-VLA-4 and anti-CXCR3 antibodies and contributed with technical advice. P.J.N. provided CCR5 blocker and contributed with scientific advice. T.Z. contributed with T-cell characterization in the CSF, D.L. designed and produced genetic retroviral sensors and contributed to the analysis of NSeq data. F.O. performed most *ex vivo* T-cell analyses, i.e. cytofluorometric characterizations, quantitative PCR and NSeq analyses. A.F. together with F.O. designed the study, coordinated the experimental work and wrote the manuscript with inputs from co-authors.

METHODS

Animals. Rats on a LEW/Crl background (*Rattus norvegicus*) were bred in the animal facilities of the University Medical Center, Göttingen (Germany) and held under standardized conditions. All animal experiments were approved by the responsible authorities (number: 209.1/211-2531-36/04 and 33.9.42502-04-016/09). Male and female animals between 6–12 weeks old were used in the EAE experiments. No differences were noted between the sexes.

Generation and culturing of T cells. $CD4^+$ T cells reactive against myelin basic protein, recombinant myelin oligodendrocyte glycoprotein (amino acids 1–120) or ovalbumin were retrovirally engineered to express eGFP or mCherry (denoted as $T_{MBP-GFP}$, $T_{OVA-GFP}$, $T_{MOG-GFP}$ and $T_{MBP-Cherry}$) as previously reported[30]. The generation of MSCV–NFAT/YFP–Cherry/H2B transduced T-cell lines ($T_{MBP-NFAT/YFP}$) is described elsewhere[10]. For the generation of $T_{MBP-Lifeact-Turquoise2}$ or $T_{MBP-Dendra2}$ cell lines, the fragment coding for the fusion protein Lifeact–mTurquoise2 (Addgene, plasmid 36201) or for the photo-switchable protein Dendra2[31] were cloned into the MCS of the murine stem cell retrovirus pMSCVpuro (Invitrogen). The generation of primary effector T-cell lines has been previously described[30]. Extraction of guinea pig MBP and production of recombinant MOG were performed as previously described[32,33]. Ovalbumin (albumin from chicken egg white grade V) was obtained from Sigma. All T-cell lines were $CD4^+$, $CD8^-$ and $\alpha\beta TCR^+$, they had an effector memory phenotype (L-selectin$^-$CD45RC^{low}CD44^{high}) and upon stimulation produced IFNγ and IL-17. Phenotype, cytokine profile, antigen specificity, pathogenicity and absence of mycoplasma contamination were verified in each cell line[30].

EAE models. Adoptive transfer EAE was induced by i.v. injection of 5×10^6 MBP- or MOG-reactive T-cell blasts (day 2 after antigen encounter). In some experiments $2–5 \times 10^6$ *ex vitro* or $0.5–2 \times 10^6$ *ex vivo* isolated T_{MBP} cells were transferred into the cisterna magna. To address the role of CNS-non-reactive T cells in a non-inflammatory situation, 5×10^6 $T_{OVA-GFP/mCherry}$ blasts were transferred as above. To investigate the behaviour of T_{OVA} cells in inflamed CNS, 2.5×10^6 $T_{OVA-GFP}$ cells were co-injected with 5×10^6 non-labelled T_{MBP} cells. For *in vivo* recording during the established phase of leptomeningeal T cell infiltration, 2×10^6 $T_{MBP-GFP}$ blasts were co-injected with 3×10^6 non-labelled T_{MBP} cells. This protocol allowed the accurate tracking of individual effector T cells.

Active EAE was induced in 8- to 12-week-old memory animals by subcutaneous antigen immunization. Memory animals were established by intraperitoneal transfer of $T_{MBP-GFP}$ cells into neonatal animals as previously described[27]. Weight and clinical scores were recorded daily (score 0, no disease; 1, flaccid tail; 2, gait disturbance; 3, complete hind limb paralysis; 4, tetraparesis; 5, death).

No statistical method was used to predetermine sample size. The experiments were not randomized. The investigators were not blinded to allocation during experiments and outcome assessment.

Cell isolation, flow cytometry and fluorescence-activated cell sorting. Isolation of fluorescently labelled T cells from the tissues has been previously described[34]. Briefly, mononuclear cells were isolated from EDTA-treated blood by density gradient. Immune cells were obtained from spinal cord meninges and parenchyma by a two-phase Percoll-density gradient. CSF was collected from the cisterna magna using a stereotactic device. The choroid plexus of the fourth and lateral ventricles was excised under a stereomicroscope by carefully pulling it off the wall of the ventricles along the tenia choroidea. Nevertheless, it cannot be excluded that adjacent meningeal tissue was excised together with the choroid plexus, thus leading to an overestimation of T_{MBP} cell numbers. Meningeal macrophages were labelled by injection of (3 kDa) Texas-Red-conjugated dextran in the cisterna magna (40 µg per rat) and isolated by density gradient 24 h later. Labelled cell populations were sorted by a FACSAria 4L SORP cell sorter (Becton Dickinson). Flow cytometry analysis was performed with a FACSCalibur operated by Cell Quest software (Becton Dickinson). Surface staining was performed by using the following mouse anti-rat monoclonal antibodies: OX-40 antigen (CD134), OX-39 antigen (CD25, IL-2 receptor α chain), CD11b/c (OX-42), $\alpha\beta TCR$-AF647 (clone R73, BioLegend), TCR Vβ 8.2 (clone R78, Santa Cruz Biotechnology), TCR Vβ 8.5 (clone B73), TCR Vβ 10 (clone G101), TCR Vβ 16.1 (clone His42), CD4-PECy7 (clone OX-35, BD Biosciences), CD62L-PE (clone OX-85, Biolegend), CD45RC-PerCPCy5.5 (clone OX-22, Abcam). All antibodies were purchased from Serotec unless indicated otherwise. Mouse IgG1κ (MOPC 31C, Sigma-Aldrich) served as isotype control; APC-labelled anti-mouse antibody (Dianova) was used as secondary antibody. For detection of the activated conformation of integrin β1, HUTS-4 antibodies[35] (0.5 mg kg^{-1}) were injected i.t. After 4 h, *ex vivo* isolated $T_{MBP-GFP}$ cells were stained with the secondary antibody. For intracellular staining, mouse anti-rat IFNγ antibodies (DB-1, Invitrogen) and rat anti-mouse IL-17–PE (BD) were used. Mouse IgG1κ (MOPC 31 C) and rat IgG1–PE were used as control. Cytofluorometric quantification of T cells was performed by relating the number of cells to a known absolute amount of fluorescent beads.

Intravital TPLSM. Intravital studies were performed during the following phases of leptomeningeal T_{MBP} cell infiltration: (1) pre-invasion, when T_{MBP} cells first appeared in leptomeningeal blood vessels but had not yet extravasated; (2) early, at the beginning of the leptomeningeal T-cell infiltration, that is, when T_{MBP} cells started to distribute within the leptomeninges but had not yet invaded the CNS parenchyma (the animals were still completely healthy); (3) established, when T_{MBP} cells had entered the leptomeninges and started to invade the CNS parenchyma (the animals began to lose body weight); (4) disease, when T_{MBP} cells invaded the CNS parenchyma (the animals showed symptoms of paralytic disease).

Surgical procedures. Animals were anaesthetized, tracheally intubated, ventilated and stabilized in a custom-made microscope stage; body temperature was regulated by a heated pad (37.5 °C). During imaging, vital parameters were registered as previously described[7]. Thoracic leptomeninges were accessed as previously described[7] by performing a laminectomy at level Th12/L1. Brainstem area was exposed as described[36]. For recording the choroid plexus, a cerebellar interhemispheric approach was performed to access the fourth ventricle. The rat was placed in a prone position with the head flexed and fixed in a custom-made stereotactic frame. The skin was incised in the midline (length approximately 2 cm) in order to expose the posterior cranial vault and first cervical vertebra. The muscle was detached using regular small scissors and bipolar forceps. The atlanto-occipital membrane was exposed between the foramen magnum and the first cervical vertebra. Afterwards, the skull was thinned out with a twist drill up to the inner cortical layer. This layer was then removed with a slightly curved forceps. Subsequently, the brainstem and the vermis were exposed and could be visualized through the dural layer. The dura was opened in the midline in a blunt fashion using bipolar forceps or a blunt micro-hooklet. The adjacent brain tissue was retracted to the side and partially reduced in size by bipolar coagulation and resection in a 30–45° angle upwards in the sagittal plane in order to enter the fourth ventricle. Upon ventricle entry, CSF and the basal part of the fourth ventricle plexus could be visualized. After each preparation fluorescently labelled dextran was injected i.v. to confirm that the choroid plexus vessels were patent.

Labelling of phagocytic cells and blood vessels. Meningeal phagocytes were labelled by i.t. injection of 3 kDa Texas-Red-conjugated Dextran 48 h after transfer. Blood vessel lumen was visualized by i.v. infusion of (2000 kDa) TRITC-labelled dextran (200 µg) before or during TPLSM recordings.

Technical equipment and processing of raw data. Time-lapse TPLSM was performed using a LSM710/Axio Examiner Z1 microscope (Carl-Zeiss Microimaging) combined with a > 2.5 Watt Ti:Sapphire Chameleon Vision II Laser device (Coherent GmbH). The excitation wavelength was tuned to 880 nm or 1010 nm and routed through a 20× water NA1.0 immersion objective W Plan Apochromat (Carl-Zeiss Microimaging). Typically, areas of 424.27 × 424.27 µm (512 × 512 pixels) width were scanned and 50–100 µm z-stacks were acquired. The interval time between sequential acquisitions was kept to 32 s. Emitted fluorescence was detected using non-descanned detectors (Carl-Zeiss Microimaging) equipped with 442/46 nm, 483/32 nm, 525/50 nm, 550/49 nm, 607/70 nm and 624/40 nm band-pass filters (Semrock Inc.). Collagen was detected by two-photon generated second-harmonic signals.

Irreversible photo-conversion of $T_{MBP-Dendra2}$ cells from green to red was achieved by irradiation of meningeal spots with UV light for 20 s. Recordings were performed at 880 nm using 483/32 nm and 550/49 nm band-pass filters. TPLSM recordings were acquired and processed by Zen 2009 Software (Carl-Zeiss Microimaging). The depth colour-coding of individual T cells in the z-plane was generated in Fiji software.

Analysis of T-cell motility. Imaris software 7.1.1 (Bitplane) was used for 3D reconstructions and 4D analysis of acquired raw data. Cells were tracked using the automated Imaris Track module with subsequent manual revision. Motility parameters including T-cell velocity (average of the instantaneous speed for each cell track), crawling duration and meandering index (ratio between total T-cell path length and the sum of the entire single displacements) were calculated as described[7,37] within a 30 min recording interval. Rolling T cells were defined as cells appearing as single or several round-shaped dots or cells moving solely in direction of the blood flow with >50 µm min^{-1} instantaneous velocity. Owing to limitations in temporal resolution of the two-photon scanning/fluorescence video microscopy equipment used, fast rolling events might have escaped our analysis[7]. The motility parameters were analysed before and after each individual treatment. The value registered before the treatments did not show any difference between the groups and therefore they were pooled together and indicated in the legends as control. Statistical evaluations were performed with GraphPad 5.0.4 (GraphPad Software).

Analysis of T-cell interactions with meningeal phagocytes/analysis of T-cell activation in vivo. Meningeal phagocytes were labelled as above. We exclusively analysed motile GFP$^+$ T cells and spots with similar density of fluorescently labelled phagocytes. Contact durations were determined by manually counting the number of

frames during which individual motile GFP$^+$ T cells were in close vicinity ($\leq$1 cell diameter distance) to resident phagocytes. As not all T cells were visible during the entire observation period of 30 min, contact frequencies were calculated as follows: the total number of phagocytes contacted by an individual T cell was divided by the total number of T-cell displacements. The obtained value was extrapolated to 30 min. For evaluation of T-cell activation *in vivo*, T cells with nuclear (translocated) or cytosolic (not translocated) NFAT sensor were quantified as previously described[10] by analysing fluorescent overlap between the green and red channel. Merged (yellow), translocated; not merged, not translocated.

Mathematical analysis of chemotactic gradients. Target migration was analysed as follows. At first, the positions of individual motile T cells and meningeal macrophages from individual TPLSM recordings were extracted. For every T$_{MBP-GFP}$ cell entering a radius of 25, 50 or 100 μm from a macrophage all the motile steps were analysed. For each step we computed the direction relative to the examined phagocyte. In particular we computed the cosine between the normalized vectors AB and AC as shown in Extended Data Fig. 6c (the letter A corresponding to the initial position of the T$_{MBP-GFP}$ cell, B to its final position and C to the position of the phagocyte). Hence, the values 1 or -1 correspond to a T$_{MBP-GFP}$ cell moving towards the meningeal phagocyte or in the opposite direction, respectively.

Analysis of T-cell migration. *Analysis of the directionality of T-cell displacement.* This analysis was performed by using standard scripts on three different time scales, the fastest sampling time ($\Delta t = 32$ s), and two slower times, $4\Delta t$ and $8\Delta t$, respectively. The three analysed time scales gave the same results; therefore, exclusively data for the fastest time scale, that is, the larger data sets, are reported.

For analysing T-cell movement in the leptomeninges, 3D displacement components were recorded. The directional analysis was split into two parts. Specifically, we first found the plane fitting the positions of all of the effector cells at all times; we then computed the normal and in-plane components of each displacement vector $\boldsymbol{u}_i$,

$$w_i = \boldsymbol{u}_i \cdot \boldsymbol{n}, \quad \boldsymbol{v}_i = \boldsymbol{u}_i - (\boldsymbol{u}_i \cdot \boldsymbol{n})\boldsymbol{n}$$

The directional migration analysis was performed separately on these two components. Here $\boldsymbol{n}$ is the unit normal to the best fitting plane.

Particularly for the sets of displacement normal components w_i, we estimated the Wiener processes maximizing the log-likelihood function. The cell displacements normal to the best-fitting plane were well approximated by Wiener processes with very small positive drifts; the typical drift was 5–8% of the average normal displacement norm, that is, $\overline{w} = \langle |w_i| \rangle$ This means that the cells moved in a random way without following any preferential direction in the n direction.

Analysis of effector T-cell movement type. The distribution of the displacement norm $|\boldsymbol{u}_i|$ was analysed. The histograms of the probability density functions for the recorded data together with the estimated Weibull, Lévy and normal (Gaussian) distributions are shown on linear scales; for all the three cases this estimation was obtained by a global maximization of the log-likelihood function. For each distribution the associated P values are reported. To compare the three hypotheses, probability plots were generated in which all of the estimated distributions were plotted against the data; the ideal line would be a straight line from (0; 0) to (1; 1). For all the cases investigated, the Weibull distribution was the most significant. This result was also confirmed by Kolmogorov–Smirnov test. Hence, for our data, the tail of the displacement-normalized distribution decayed exponentially (Weibull distribution) and it was not well approximated by a polynomial decay typical of the Lévy distribution. Considering that (1) there was no evidence of preferential directions, and (2) the displacement-norm tail decayed in an exponential way, we concluded that the effector T cells moved in a Brownian random walk.

Interference with integrin signalling. Intravital studies were performed during the early and established phases of leptomeningeal TMBP infiltration. To block integrin-mediated binding, a neutralizing mouse anti-rat monoclonal antibody against VLA-4 (anti-CD49d, clone TA-2)[38] and/or against CD11a (integrin αL, anti-LFA-1, clone WT.1, Serotec) was applied in the cisterna magna before or during intravital imaging at a single dose of 1 mg kg^{-1}. After recording, *ex vivo* isolated T cells were tested by flow cytometry for antibody saturation.

The effect of integrins on T cell motility in the leptomeninges in the absence of flow was investigated removing the dura mater and the subarachnoidea during intravital imaging. The subarachnoidal structures were left intact. Then, 30 min TPLSM recordings were performed before and after *in situ* application of VLA-4 and LFA-1 monoclonal antibodies (20 μg each per rat).

Interference with chemokine signalling. Intravital studies were performed during the early and established phases of leptomeningeal T$_{MBP}$ infiltration. Pertussis toxin A oligomer (10 μg kg^{-1}) (PTX, an exotoxin that blocks G-protein-coupled Gα$_i$ signalling and therefore acts as global chemokine inhibitor; List biological laboratories), 1 mg kg^{-1} Met-RANTES, 1 mg kg^{-1} hamster anti-rat CXCR3

monoclonal antibody (clone XR3.2), 0.5 mg kg^{-1} AMD3100 (also known as plerixafor) (Sigma/Genzyme) or PBS were applied in the cisterna magna before or during intravital imaging. These monoclonal antibodies or blocking agents were shown to be effective *in vivo* in EAE models[39–41]. The dose selected for the *in vivo* experiments was able to block T-cell migration in chemotaxis assays. In some experiments, pertussis toxin B oligomer, Armenian hamster IgG or mouse IgG1 isotype antibody (Abcam) were used as controls. To confirm the efficacy of the treatments after the imaging session, *ex vivo* isolated effector T cells were tested in chemotaxis assays towards the respective chemokines.

Intravital fluorescence microscopy. For fast-acquisition fluorescence video microscopy, a LSM710/Axio Examiner Z1 microscope (Carl-Zeiss Microimaging) was used in combination with an HXP120C illuminator routed through a 20× water NA1.0 immersion objective W Plan Apochromat (Carl-Zeiss Microimaging). Acquisition rate was 7–10 frames per minute. Fluorescent signals were detected using a Zeiss AxioCam HSM video camera. Mechanical hyperventilation was induced by increasing the ventilation rate in 200 g rats from 81 to 100 breaths per minute (bpm) equivalent to the ventilation rate of 100 g animals. Cardiac vagolytic effect was achieved by subcutaneous administration of the muscarinic receptor antagonist methylscopolamine (0.05 mg kg^{-1}) 30 min before imaging[42].

Block of T-cell transport from the fourth ventricle to the subarachnoidal space. Two different procedures were performed. CSF flow obstruction was obtained by injecting growth-factor-reduced Matrigel (BD Bioscience; 160 μl for 140–170 g animals) intracisternally as previously described[8,43]. To assess the success of the Matrigel obstruction, we mixed Evans blue dye into the Matrigel and visually confirmed that the Matrigel not only enclosed the medulla oblongata but also completely filled the entire fourth ventricle (Extended Data Fig. 2a, left panel). Visual inspection of Matrigel localization in and around the fourth ventricle was performed in all animals of each experiment.

A spinal cord window was opened at the cervical level before intravital imaging. Then, the dura was removed and a small hole inserted in the arachnoidea, allowing the CSF to leak out. The CSF efflux induced a collapse of the subjacent thoracic subarachnoidal space and thereby abolished the CSF flow in this area (Extended Data Fig. 2c, d).

Intrathecal injection of T cells. Effector T cells were either cultured *in vitro* and injected on day 2 (activated cells) or on day 6 (resting cells) after antigen stimulation, or isolated *ex vivo* from spinal cord parenchyma or CSF. Effector T cells from parenchyma were purified by a two layer OptiPrep (Axis-Shield PoC) density gradient. To block chemokine or integrin signalling T cells were incubated with either (1) PTX (0.2 μg ml^{-1}); (2) anti-rat monoclonal antibodies against VLA-4 (0.4 mg ml^{-1}) or LFA-1 (0.4 mg ml^{-1}); (3) mouse IgG2a (0.4 mg ml^{-1}) isotype control, or (4) cell culture medium alone for 1 h at 37 °C and washed thoroughly before injection. T$_{MBP-GFP}$ or T$_{OVA-Cherry}$/T$_{OVA-GFP}$ cells (0.8–2 × 10^6 *ex vivo* cells or 5 × 10^6 *in vitro* cultured cells) were injected into the cisterna magna in a total volume of 40–50 μl. In some experiments T cells were injected by lumbar puncture at the level L3–L4 as described[44]. Cells pre-incubated with antibody were tested by flow cytometry for antibody saturation before injection and after retrieval.

RNA extraction, cDNA library preparation and RNA-seq. RNA extraction, cDNA library preparation and RNA sequencing were undertaken as previously described[45]. Total RNA was purified using the TRIzol protocol (Invitrogen) from 6 different samples: *in vitro* T$_{MBP-GFP}$ cell blasts (20 h after antigen encounter), *in vitro* T$_{MBP-GFP}$ resting T cells (day 6 after antigen encounter); *ex vivo* T$_{MBP-GFP}$ cells from blood, CSF, spinal cord leptomeninges and parenchyma collected 3 days after transfer. Between 200,000–400,000 T$_{MBP-GFP}$ cells were sorted from each sample with a BD FACSAria 4L SORP with more than 98% purity. Three different biological replicates were prepared for each sample. Five to seven animals were pooled for each *ex-vivo* sample. Library preparation for RNA-seq was performed using the TruSeq RNA Sample Preparation Kit (Illumina) starting from 500 ng of total RNA. Single read (45 bp) sequencing was conducted using a HiSeq 2000 (Illumina). Fluorescence images were transformed to BCL files with the Illumina BaseCaller software. Samples were demultiplexed to FASTQ files with CASAVA. Sequencing quality was checked and approved via the FastQC software. Sequences were aligned to the genome reference sequence of *Rattus norvegicus* using the STAR alignment software[46] allowing for 2 mismatches within 45 bases. Subsequently, conversion of resulting SAM files to sorted BAM files, filtering of unique hits and counting was conducted with SAMtools[47] and HTSeq[48]. Data was preprocessed and analysed in the R/Bioconductor environment using the DESeq2 package[49]. Candidate genes were filtered to a minimum of twofold change and FDR-corrected P value < 0.05. Gene annotation was performed using *Rattus norvegicus* entries from Ensembl v78 via the biomaRt package[50]. KEGG pathway analysis was performed by using The Database for Annotation, Visualization and Integrated Discovery (DAVID)[51].
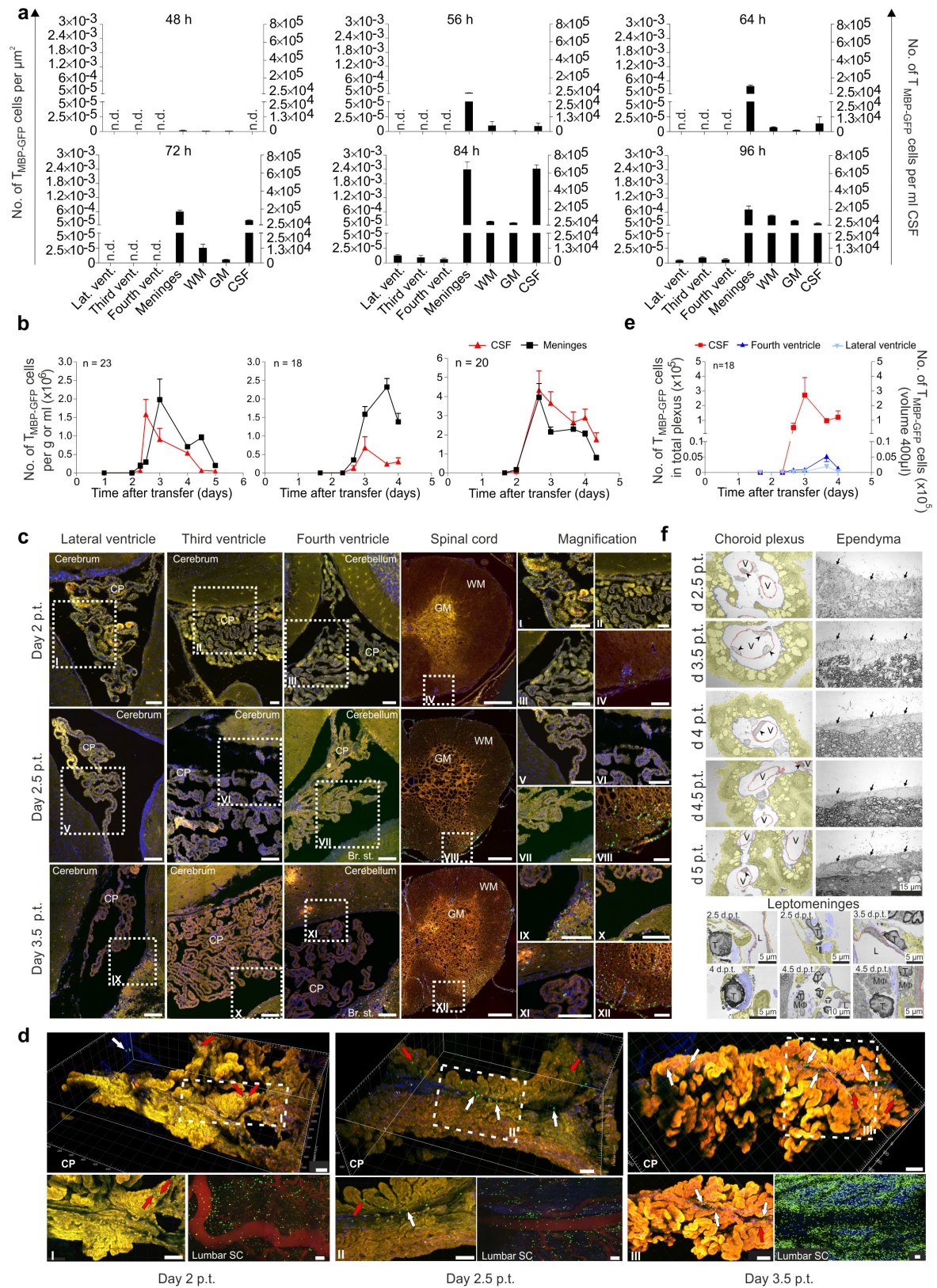
Quantitative PCR. mRNA extraction, cDNA synthesis and quantitative PCR were performed as described[18]. The following rat-specific primers and FAM-TAMRA-labelled probes not previously described[7,18,52] were used. Vascular cell adhesion molecule 1 (VCAM-1): forward, 5′-TGAGGCTGGAATTAGCAAAAAAT-3′, reverse, 5′-TTAGATGGGAAGACTGTAAGTTGTATG-3′, probe: 5′-CTGATTAT CCAAGGCTCTT-3′; intercellular adhesion molecule 1 (ICAM-1): forward, 5′-GAAGACAGCAGACCACTGTGCTT-3′, reverse, 5′-CTCGCTCTGGGGAA CGAATACA-3′, probe: 5′-ACTGTGGCACCACGC-3′; fibronectin transcript-1 (fn-1): forward, 5′-TGATCTTTGAGGAACATGGCTTT-3′, reverse, 5′-GCAGGT ATGGTCTTGGCCTAAG-3′, probe: 5′-AACCACGCCACCCACTGCGG-3′; fibronectin transcript-2 (fn-1): forward, 5′-GAGCTTCCCCAACTGGTTAACC-3′, reverse, 5′-GAACTGTGGAGGGAACATCCAA-3′, probe, 5′-CCACACCCCAA TCTTCATGGACCAGA-3′. Unless otherwise stated, β-actin was used as house-keeping gene.

In vitro **proliferation assay of T cells.** Amplification of *ex vivo* or *in vitro* isolated $T_{MBP-GFP}$ cells upon antigen stimulation was tested by flow cytometry as previously described[18].

Histology and immunohistochemistry. Histological analysis was performed as described[34] using the following antibodies: rabbit anti-CXCL-11 (Biorbyt), mouse anti-rat RECA-1 (Abcam), guinea-pig anti-Iba-1 (Synaptic Systems), mouse anti-rat OX-6 (rat RT1B MHC class II antigen, Serotec), mouse anti-alpha-smooth muscle actin (DAKO). eGFP was enhanced by GFP-Atto 488 (Chromotek). Alexa Fluor568 goat anti-rabbit IgG, Alexa Fluor647 goat anti-mouse IgG (both from Invitrogen), Alexa Fluor647 donkey anti-guinea pig (Dianova) were used as control. Images were acquired using either a Zeiss Axio Observer fluorescence Microscope equipped with a 10× Air Objective or a Zeiss LSM700 confocal microscope equipped with a 40× or 63× Zeiss objective. For histological quantification of $T_{MBP-GFP}$ cells in CNS areas, consecutive cryosections (16 μm) were acquired with a VS120 Virtual Slide Microscope (Olympus) equipped with a 10x objective. Counting of $T_{MBP-GFP}$ cells and area measurements were performed with Fiji software[53]. For CNS explant imaging, lumbar spinal cord and fourth ventricle choroid plexus were prepared. Images were acquired by TPLSM. For detection of integrin ligands *in vivo* on leptomeningeal structures dura mater and arachnoidea were removed leaving the subarachnoidal structures intact. PE-labelled VCAM or ICAM antibodies (BioLegend) and the respective isotype controls were then incubated *in situ* for 30 min before confocal acquisition.

Electron Microscopy. Animals were perfused with saline followed by a fixative containing 4% PFA and 1% glutaraldehyde for ultrastructural analysis and 4% PFA and 0.1% glutaraldehyde for immuno-electron microscopy. After post-fixation the spinal cord was cut into 60 μm sections using a Leica vibrating microtome. For immuno-electron microscopy, goat anti-GFP antibody (Acris antibodies) was used to detect the GFP signal. Biotinylated rabbit anti-goat antibody (Sigma Aldrich) was used as secondary antibody. The sections were then incubated with ExtrAvidin (Sigma-Aldrich) and stained with diaminobenzidine (DAB, Sigma-Aldrich) to achieve an electron dense precipitate. Omitting primary antibodies resulted in the absence of staining. After that, the sections were stained in 0.5% osmium tetroxide, dehydrated and embedded in durcupan (Sigma-Aldrich). Regions of interest were identified by light microscopy, cut and transferred onto blocks of resin to obtain ultra-thin sections using an Ultramicrotome (Leica). Ultra-thin sections were transferred on formvar-coated copper grids and stained using lead citrate. Ultrastructural analysis was performed using a Zeiss SIGMA electron microscope equipped with a STEM detector and ATLAS software.

30. Flügel, A., Willem, M., Berkowicz, T. & Wekerle, H. Gene transfer into CD4$^+$ T lymphocytes: green fluorescent protein-engineered, encephalitogenic T cells illuminate brain autoimmune responses. *Nature Med.* **5,** 843–847 (1999).
31. Gurskaya, N. G. *et al.* Engineering of a monomeric green-to-red photoactivatable fluorescent protein induced by blue light. *Nature Biotechnol.* **24,** 461–465 (2006).
32. Eylar, E. H., Kniskern, P. J. & Jackson, J. J. Myelin basic proteins. *Methods Enzymol.* **32,** 323–341 (1974).
33. Adelmann, M. *et al.* The N-terminal domain of the myelin oligodendrocyte glycoprotein (MOG) induces acute demyelinating experimental autoimmune encephalomyelitis in the Lewis rat. *J. Neuroimmunol.* **63,** 17–27 (1995).
34. Flügel, A. *et al.* Migratory activity and functional changes of green fluorescent effector cells before and during experimental autoimmune encephalomyelitis. *Immunity* **14,** 547–560 (2001).
35. Luque, A. *et al.* Activated conformations of very late activation integrins detected by a group of antibodies (HUTS) specific for a novel regulatory region (355–425) of the common β1 chain. *J. Biol. Chem.* **271,** 11067–11075 (1996).
36. Siffrin, V. *et al.* Differential immune cell dynamics in the CNS cause CD4$^+$ T cell compartmentalization. *Brain* **132,** 1247–1258 (2009).
37. Kawakami, N. *et al.* Live imaging of effector cell trafficking and autoantigen recognition within the unfolding autoimmune encephalomyelitis lesion. *J. Exp. Med.* **201,** 1805–1814 (2005).
38. Issekutz, T. B. Inhibition of in vivo lymphocyte migration to inflammation and homing to lymphoid tissues by the TA-2 monoclonal antibody. A likely role for VLA-4 in vivo. *J. Immunol.* **147,** 4178–4184 (1991).
39. Sporici, R. & Issekutz, T. B. CXCR3 blockade inhibits T-cell migration into the CNS during EAE and prevents development of adoptively transferred, but not actively induced, disease. *Eur. J. Immunol.* **40,** 2751–2761 (2010).
40. Matsui, M. *et al.* Treatment of experimental autoimmune encephalomyelitis with the chemokine receptor antagonist Met-RANTES. *J. Neuroimmunol.* **128,** 16–22 (2002).
41. Meiron, M., Zohar, Y., Anunu, R., Wildbaum, G. & Karin, N. CXCL12 (SDF-1alpha) suppresses ongoing experimental autoimmune encephalomyelitis by selecting antigen-specific regulatory T cells. *J. Exp. Med.* **205,** 2643–2655 (2008).
42. Carnevali, L. *et al.* Vagal withdrawal and susceptibility to cardiac arrhythmias in rats with high trait aggressiveness. *PLoS ONE* **8,** e68316 (2013).
43. Slobodian, I., Krassioukov-Enns, D. & Del Bigio, M. R. Protein and synthetic polymer injection for induction of obstructive hydrocephalus in rats. *Cerebrospinal Fluid Res.* **4,** 9 (2007).
44. De la Calle, J. L. & Paino, C. L. A procedure for direct lumbar puncture in rats. *Brain Res. Bull.* **59,** 245–250 (2002).
45. Cabeza, R. *et al.* An RNA sequencing transcriptome analysis reveals novel insights into molecular aspects of the nitrate impact on the nodule activity of Medicago truncatula. *Plant Physiol.* **164,** 400–411 (2014).
46. Dobin, A. *et al.* STAR: ultrafast universal RNA-seq aligner. *Bioinformatics* **29,** 15–21 (2013).
47. Li, H. *et al.* The Sequence Alignment/Map format and SAMtools. *Bioinformatics* **25,** 2078–2079 (2009).
48. Anders, S., Pyl, P. T. & Huber, W. HTSeq–a Python framework to work with high-throughput sequencing data. *Bioinformatics* **31,** 166–169 (2015).
49. Anders, S. & Huber, W. Differential expression analysis for sequence count data. *Genome Biol.* **11,** R106 (2010).
50. Durinck, S. *et al.* BioMart and Bioconductor: a powerful link between biological databases and microarray data analysis. *Bioinformatics* **21,** 3439–3440 (2005).
51. Huang, W., Sherman, B. T. & Lempicki, R. A. Systematic and integrative analysis of large gene lists using DAVID bioinformatics resources. *Nature Protocols* **4,** 44–57 (2009).
52. Odoardi, F. *et al.* Instant effect of soluble antigen on effector T cells in peripheral immune organs during immunotherapy of autoimmune encephalomyelitis. *Proc. Natl Acad. Sci. USA* **104,** 920–925 (2007).
53. Schindelin, J. *et al.* Fiji: an open-source platform for biological-image analysis. *Nature Methods* **9,** 676–682 (2012).
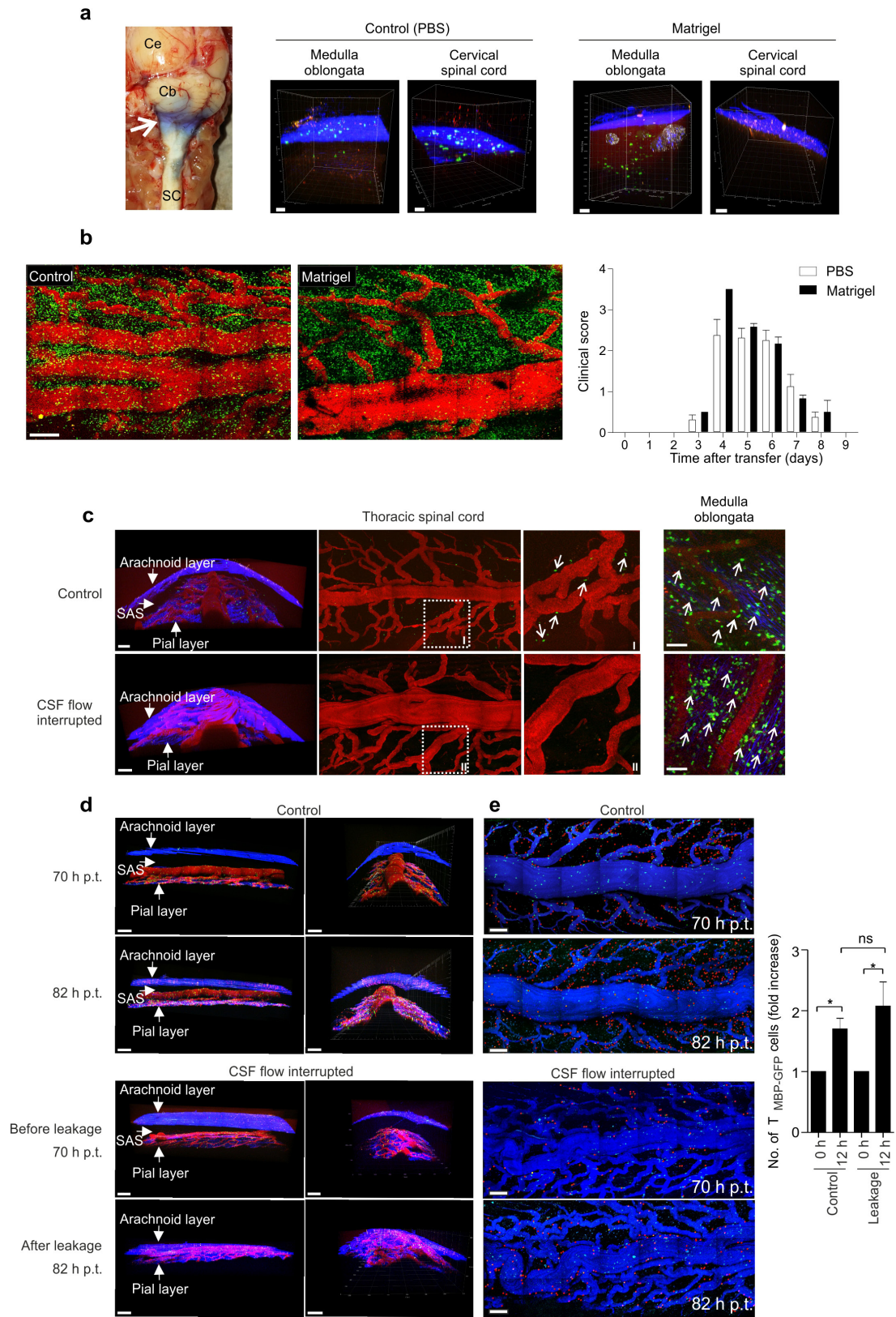
Extended Data Figure 1 | See next page for figure caption.

Extended Data Figure 1 | T$_{MBP}$ cells enter the CSF from the leptomeninges. a, T$_{MBP}$ cell entry into the CNS compartments. T$_{MBP–GFP}$ cells were quantified by histological analysis in the choroid plexus of all four ventricles (1st–4th vent) and spinal cord (meninges, white matter (WM) and grey matter (GM)) and by flow cytometry in the CSF. Histology of 6–27 consecutive slices per compartment. n.d., not detectable. Representative experiment ± s.e.m. from 2 independent experiments ($n = 12$) from days 1.5–5 after transfer. **b**, Accumulation of T$_{MBP–GFP}$ cells in the CSF and leptomeninges occurs simultaneously. Numbers of T$_{MBP–GFP}$ cells (flow cytometry) in meninges and CSF. Results of 3 independent experiments. Data are mean ± s.d. of 2–4 animals per time point ($n = 61$). **c**, T$_{MBP}$ cells accumulate in the leptomeninges but not in the choroid plexus. Confocal laser scanning microscopy of fixed tissue sections of the lateral, third and fourth ventricles and fluorescence microscopy images of lumbar spinal cord sections. Images were recorded from the same animal for each time point. Br. st., brain stem; green, T$_{MBP–GFP}$ cells; blue, DAPI counterstain of nuclei. Right (I–XII), magnifications of areas of interest. Representative images of 14 different time points from days 1.5–5 after T-cell transfer. **d**, Localization of T$_{MBP}$ cells in choroid plexus explants compared to spinal cord leptomeninges. Original TPLSM images and 3D reconstructions of explanted choroid plexus of the fourth ventricle. The corresponding lumbar spinal cord leptomeninges (lumbar SC) was acquired before explantation of the choroid plexus.
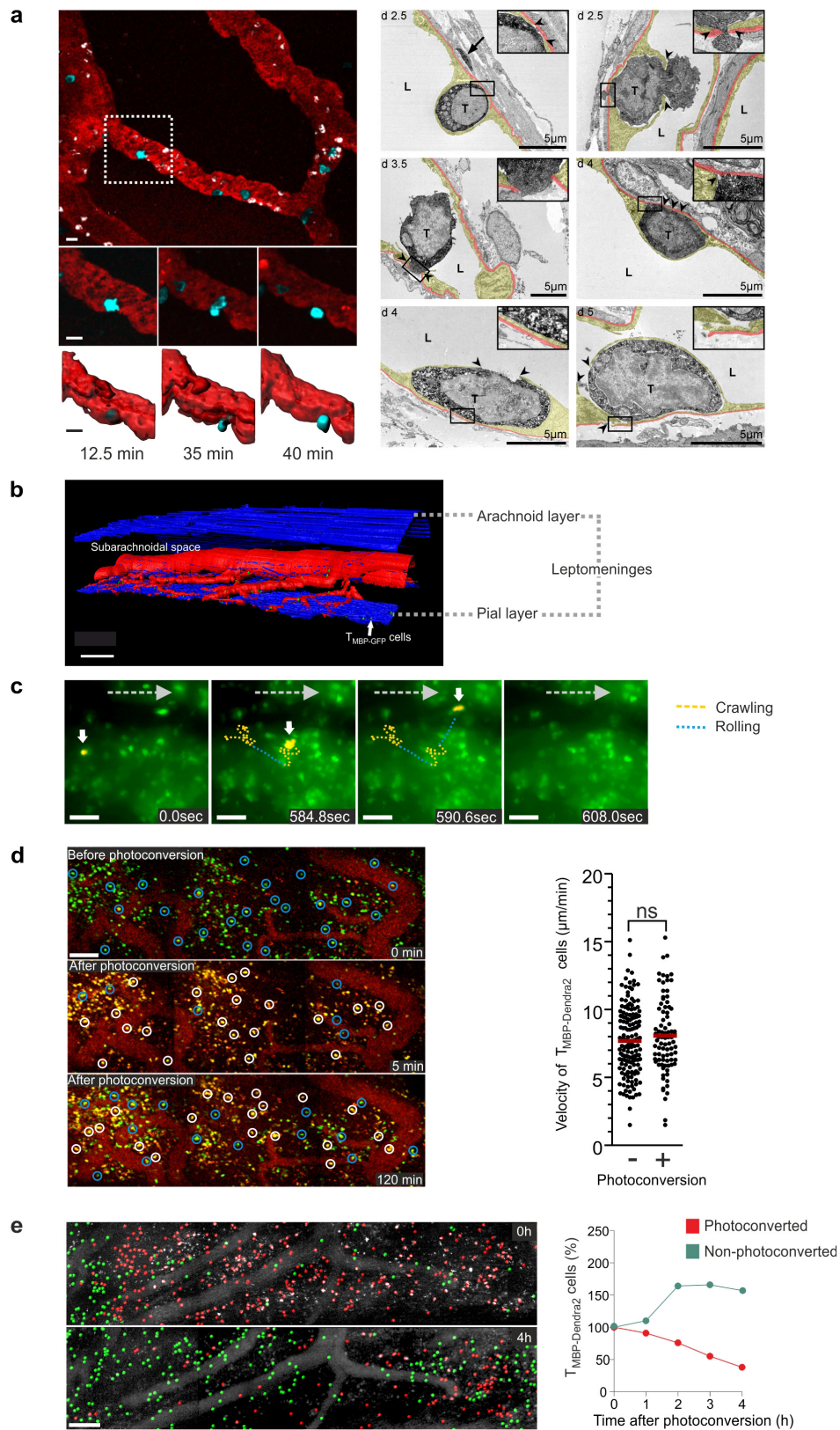
Green, T$_{MBP–GFP}$ cells; red, meningeal blood vessels; blue, collagen. Few T$_{MBP–GFP}$ cells can be detected within the choroid plexus tissues compared to the leptomeninges of the spinal cord. Red arrows, T$_{MBP–GFP}$ cells within the choroid plexus stroma; white arrows, T$_{MBP–GFP}$ cells outside of the choroid plexus tissue. Representative pictures of 2 independent experiments ($n = 10$). Scale bars, 100 μm (**c**, **d**). **e**, T$_{MBP}$ cells accumulate in the CSF before appearing in the choroid plexus. Quantification of T$_{MBP–GFP}$ cells from the choroid plexus of the fourth and lateral ventricles and from the CSF (flow cytometry). Means ± s.d. Representative data of 3 independent experiments including 2–4 animals per time point. **f**, Anti-GFP immuno-electron microscopy confirms the scarcity of T$_{MBP}$ cells in the choroid plexus. Upper left, choroid plexus of the fourth ventricle. The choroid plexus epithelial cells are colour-coded in yellow. The lamina propria between epithelial basal lamina (blue) and vascular basal lamina (red) is filled with loose connective tissue and meningeal fibroblasts. Arrow heads, endothelial nuclei of cross sectioned vessels (V). Top right, ependyma. The surface of the ventricular ependyma (arrows) appears smooth and continuous with numerous ciliary processes. No T$_{MBP}$ cells could be detected for any of the observed time points after T-cell transfer. Lower panel, leptomeninges. T$_{MBP–GFP}$ cells (T) are marked by typical black grains of DAB. Yellow, resident leptomeningeal cells; blue, bundles of collagen fibres; red, vascular endothelial basal laminas. MΦ, macrophages; L, vascular lumen.

Extended Data Figure 2 | See next page for figure caption.

Extended Data Figure 2 | Interference with T$_{MBP}$ cell transport within the CSF does not inhibit their accumulation in the spinal cord and clinical EAE. a, T$_{MBP}$ cell transport from the cisterna magna to the subarachnoidal space of the spinal cord is effectively blocked by Matrigel. Left, macroscopic image of the cisterna magna and the adjacent parts of the CNS after injection of Matrigel mixed with Evans blue dye. Cb, cerebellum; Ce, cerebrum; SC, spinal cord. Arrow, cisterna magna filled with blue-stained Matrigel. Right, PBS or Matrigel was injected in the cisterna magna of naive animals. T$_{MBP–GFP}$ cells were injected 24 h later intra-cisternally. TPLSM of the medulla oblongata and the cervical spinal cord was performed 6 h after the T$_{MBP–GFP}$ cell injection. Shown are 3D reconstructions of the TPLSM recordings. Notably, in Matrigel-injected animals the T$_{MBP}$ cells remained localized in the cisterna magna but did not reach the cervical spinal cord, indicating that the Matrigel efficiently blocked the migration of cells from the cisterna to the subjacent leptomeninges. In controls (PBS-injected animals), T$_{MBP}$ cells readily reached the leptomeninges of the cervical spinal cord. Green, T$_{MBP–GFP}$ cells; blue, collagen. Scale bars, 50 μm. **b,** Leptomeningeal T-cell infiltration and clinical disease are not impaired after Matrigel blockage. Matrigel was injected into the cisterna magna 2 days after i.v. transfer of T$_{MBP–GFP}$ cells. PBS i.t.-injected animals were used as control. Left, TPLSM recordings of thoracic leptomeninges 3.5 days after transfer. Representative data of 2 independent experiments. Scale bar, 200 μm. Right, clinical score assessment. Representative data of 2 independent experiments including 4 animals per treatment ($n = 16$). Mean ± s.e.m. **c,** T$_{MBP}$ cell transport from the cisterna magna to the subarachnoidal space of the spinal cord is effectively blocked by interrupting the CSF flow. Resting T cells (5×10^6) were injected into the cisterna magna either in control animals (upper panel) or in animals where the CSF flow was interrupted by introducing a CSF leakage at the level of the cervical spinal cord (lower panel). The efflux of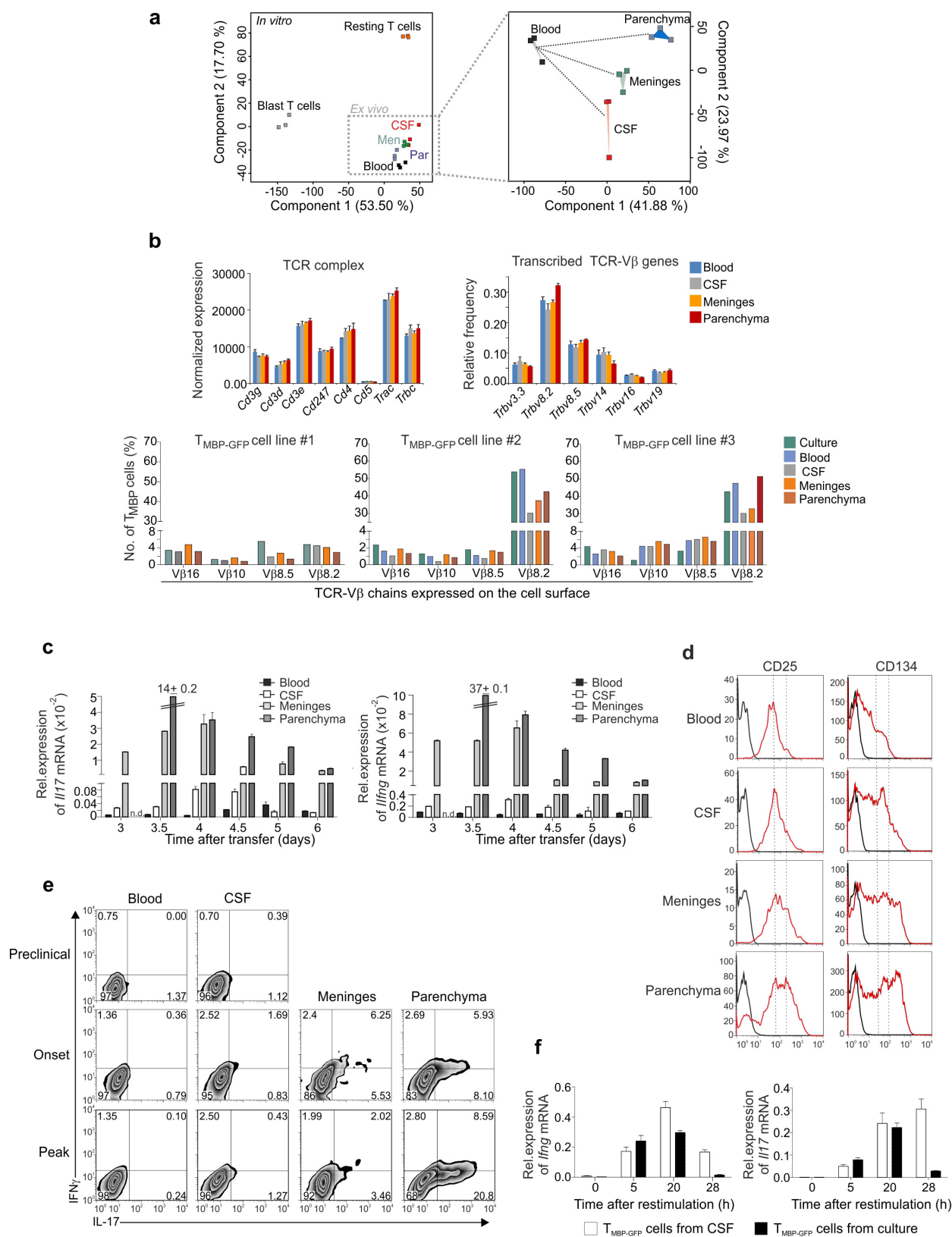 the CSF induced a collapse of the subjacent thoracic subarachnoidal space (SAS) and thereby abolished the CSF flow in this area. TPLSM recordings of the thoracic spinal cord and of the medulla oblongata 6 h after i.t. injection. Depicted are 3D reconstructions of TPLSM recordings of the thoracic spinal cord leptomeninges, overviews of the same area with magnifications of areas of interest (I, II) and overviews of the medulla oblongata. Green, T$_{MBP–GFP}$ cells; red, blood vessels; blue, collagen. Arrows, representative T$_{MBP–GFP}$ cells. Scale bars, 300 μm for thoracic spinal cord and 50 μm for medulla oblongata. Note that in the animals with disrupted CSF flow, no T$_{MBP}$ cells were detectable at the level of the spinal cord despite the high number of T$_{MBP}$ cells in the medulla oblongata indicating that the leakage completely blocked the transport of cells from the cisterna magna to the subjacent spinal cord leptomeninges. **d, e,** Interrupting the CSF flow does not impair T$_{MBP}$ cell accumulation in the spinal cord leptomeninges. **d,** Shown are 3D reconstructions of TPLSM recordings of the thoracic spinal cord leptomeninges after i.v. transfer of T$_{MBP–GFP}$ cells. Images before (70 h after transfer) and after introducing a CSF leakage at the level of the cervical spinal cord (82 h after transfer). Animals with intact flow were used as control. Green, T$_{MBP–GFP}$ cells; red, meningeal blood vessels; blue, collagen. Scale bars, 300 μm. **e,** Left, TPLSM overviews of the thoracic spinal cord leptomeninges. The numbers of T$_{MBP–GFP}$ cells that had emigrated from the local vessels into the leptomeningeal milieu (red false colours) within the 12 h interval did not differ between controls and 'CSF flow interrupted' animals. Green and red marks (overlaid red dots), T$_{MBP}$ cells located inside or outside the vessels, respectively; blue (false colour), meningeal blood vessels. Scale bars, 200 μm. Right, relative increase of T$_{MBP–GFP}$ cells located in the extravascular compartment at the indicated time points during imaging either in control animals or in animals where the CSF was interrupted (leakage). Representative data of 3 independent experiments (Kruskal–Wallis ANOVA followed by Dunn's multiple comparison test, *$P < 0.05$). Mean ± s.d.

Extended Data Figure 3 | See next page for figure caption.

Extended Data Figure 3 | T$_{MBP}$ cells entering the leptomeningeal milieu from local vessels become detached and float within the CSF. a, T$_{MBP}$ cell extravasation from the leptomeningeal vessels. Left, TPLSM during the pre-invasion phase. Representative T$_{MBP}$ cell diapedesis. Depicted is a very early transmigration event, that is, the majority of both T$_{MBP}$ cells and CD11b$^+$ myeloid cells are located inside the vascular lumina. Red, meningeal blood vessels; blue, T$_{MBP–Lifeact–Turquoise2}$ cells; white, CD11b$^+$ myeloid cells labelled by i.v. administration of fluorescently conjugated anti-CD11b monoclonal antibody during imaging. Scale bars, 10 μm. Right, immuno-electron microscopy of T$_{MBP}$ cell extravasations observed at the indicated time points after transfer. Yellow, endothelial layer of leptomeningeal vessels; red, endothelial basal lamina. T$_{MBP–GFP}$ cells are marked by cytoplasmic DAB. Extravasating T$_{MBP}$ cells were often found to be surrounded by endothelial processes. Thereby, notable abluminal or luminal gaps (arrow heads) of the endothelial layer were frequently observed. Representative electron micrographs at the indicated time points. L, vascular lumen; T, T cells. **b**, Surface-rendered 3D reconstruction of the meningeal compartment. TPLSM recording in the early phase of leptomeningeal T$_{MBP}$ cell infiltration. Red, meningeal blood vessels; green, T$_{MBP–GFP}$ cells; blue, collagen. Scale bar, 300 μm. **c**, Visualization of a T$_{MBP}$ cell detaching from the leptomeninges into the CSF. Intravital video-microscopy during the established phase of leptomeningeal T$_{MBP}$ cell infiltration depicts a T$_{MBP–GFP}$ cell (false colour

yellow, indicated by the white arrow) in the process of detachment from the pial surface. Yellow and blue lines, crawling and rolling steps, respectively; dotted grey arrows, direction of the CSF flow. Scale bars, 50 μm. **d**, *In situ* light exposure induces efficient and high contrast photoconversion of T$_{MBP–Dendra2}$ cells without influencing T-cell motility. Images show representative TPLSM leptomeningeal overviews during established leptomeningeal T$_{MBP}$ cell infiltration before (0 min), 5 min, and 120 min after photoconversion. Red, meningeal blood vessels; green, non-photoconverted T$_{MBP–Dendra2}$ cells; yellow, photoconverted T$_{MBP–Dendra2}$ cells; blue and white circles, representative non-photoconverted or photoconverted T$_{MBP–Dendra2}$ cells, respectively. Plotted are mean velocities of individual T$_{MBP–Dendra2}$ cells before and 2 h after photoconversion. Data refer to 30 min time-lapse recordings. Mean values from 239 cells from at least 3 independent experiments (two-tailed Mann–Whitney *U*-test). **e**, Rapid turnover of effector T cells in the leptomeninges. Intravital TPLSM recordings on leptomeninges during the established phase of leptomeningeal T$_{MBP}$ cell infiltration. Images show distribution of T$_{MBP–Dendra2}$ cells before or 4 h after photoconversion. For better visualization, red and green dots were overlaid onto photoconverted and non-photoconverted T cells, respectively. Grey (false colour), vessel lumen. Scale bar, 100 μm. Right, relative changes of photoconverted versus non-photoconverted T$_{MBP–Dendra2}$ cells over time obtained from intravital recordings. Representative data of at least 3 independent experiments.
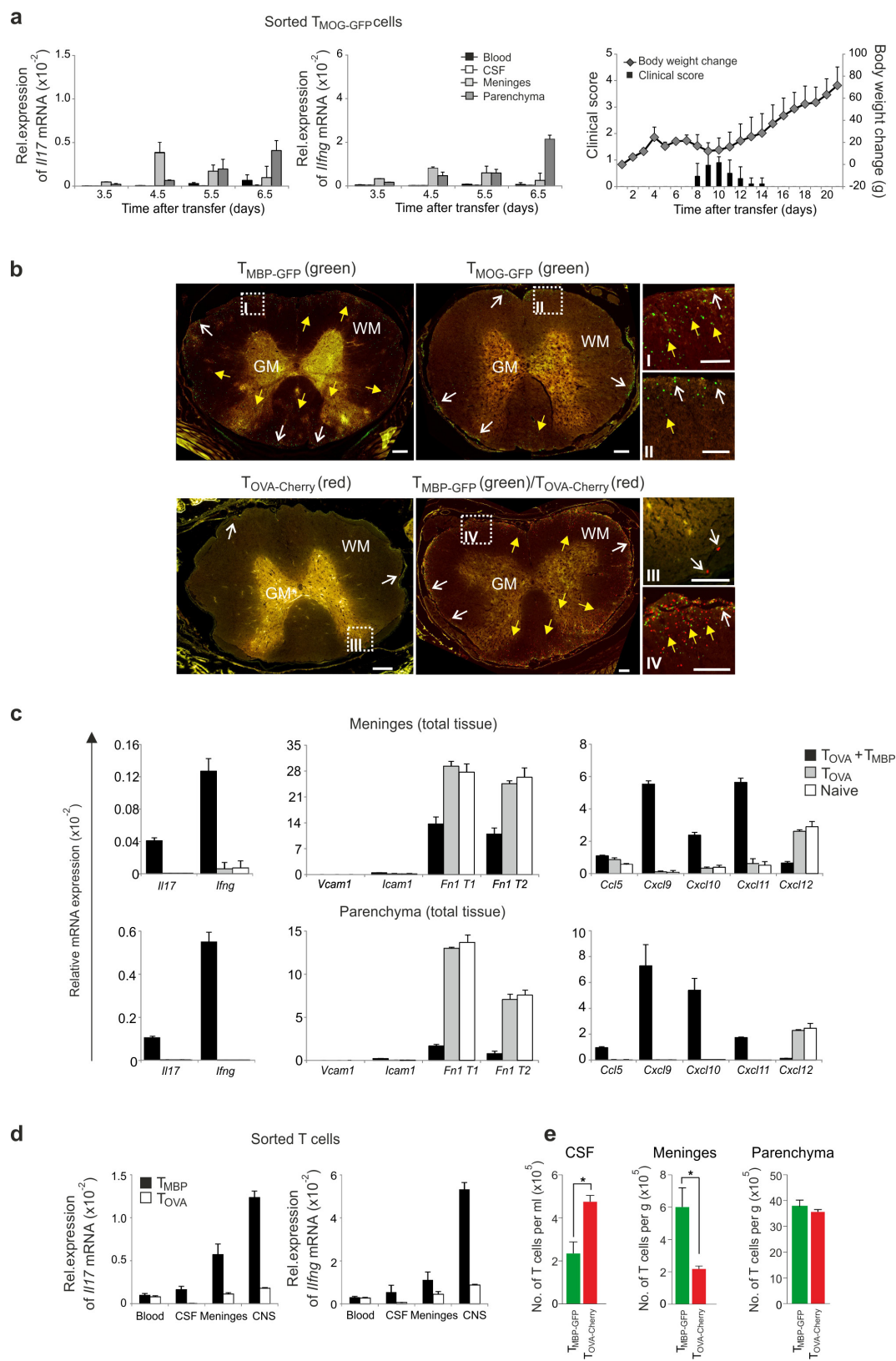
Extended Data Figure 4 | See next page for figure caption.

Extended Data Figure 4 | CSF-derived T$_{MBP}$ cells do not represent a specialized sub-population compared to T$_{MBP}$ cells in the meninges and CNS parenchyma but they display a lower activation profile.
a, Similarities in transcriptome profiles between T$_{MBP}$ cells in blood, CSF, leptomeninges and CNS parenchyma. RNA-seq of T$_{MBP–GFP}$ cells sorted from blood, meninges (Men), CSF and CNS parenchyma (Par) 3 days after transfer and on *in vitro* cultured T$_{MBP–GFP}$ cells sorted 20 h and 6 days after antigenic stimulation (blast and resting T cells, respectively). Principal component analysis of the transcriptomes for all six T cell populations (left) and for the four *ex vivo* populations (right) show similar profiles of T$_{MBP–GFP}$ cells in the CSF and the other CNS compartments compared to blood and culture. Numbers in parentheses, proportion of total variability calculated for each principal component. Each data point represents a biological replicate. **b**, T$_{MBP}$ cells display similar TCR repertoires in the CNS compartments. Top, RNA-seq as in **a**. Normalized expression of invariant TCR complex components (left) and mean frequencies of the TCR Vβ genes (right) determined as the proportion of RNA-seq reads that map to certain Vβ segments among all reads mapping to the entire set of 24 rat Vβ segments. Shown are the 6 most abundant Vβ segments. Bottom, T$_{MBP–GFP}$ cells from culture (4 days after antigen stimulation), blood, or from the indicated CNS compartments on day 4 after T-cell transfer. Expression (flow cytometry) of different TCR Vβ chains. Percentages of the different Vβ chains for three different T$_{MBP}$ cell lines.
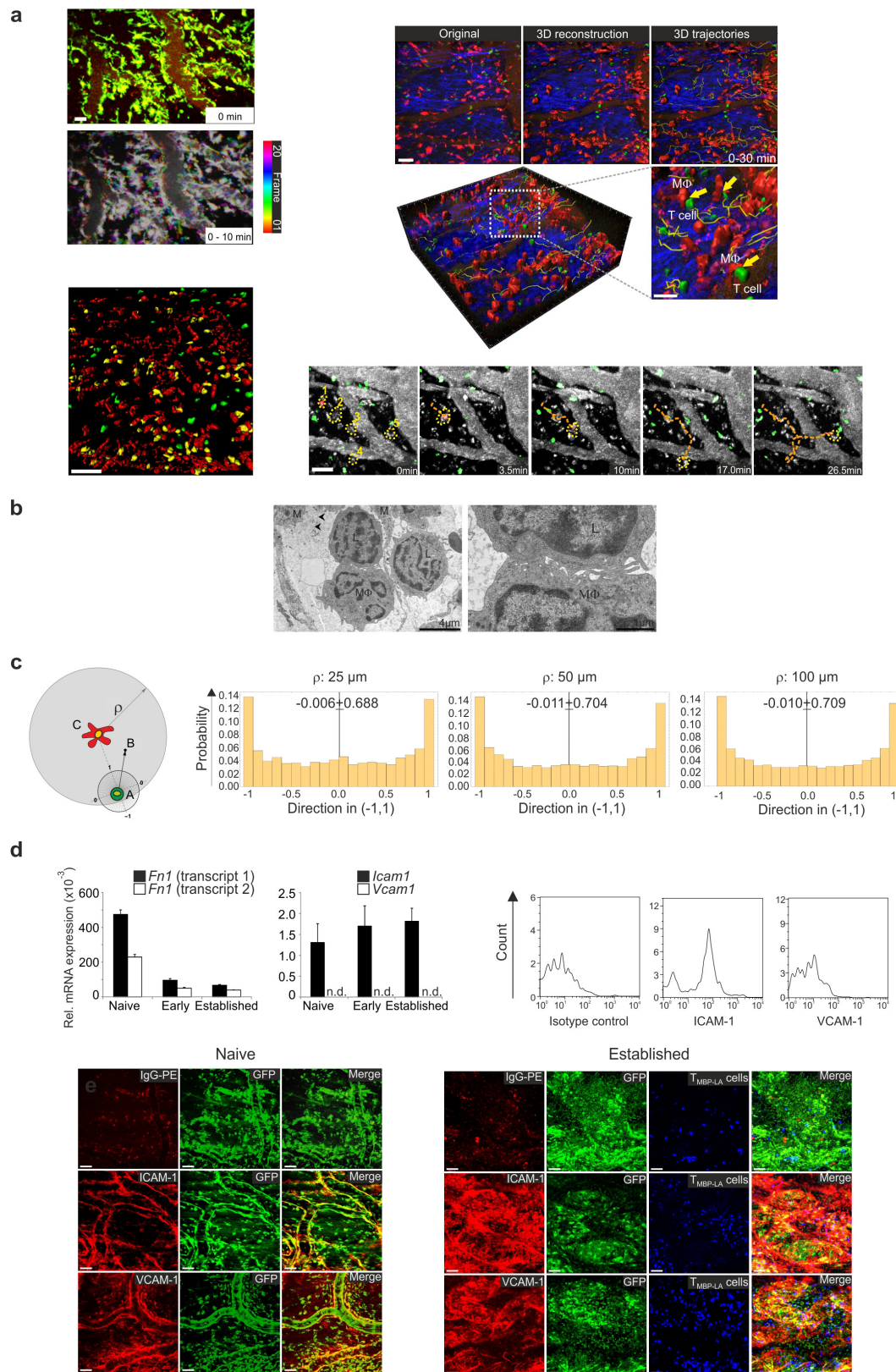
Ex vivo cell staining containing pooled cells from the respective organs of 3–4 animals ($n = 10$). **c–e**, T$_{MBP}$ cells within blood and CSF are not activated in contrast to T$_{MBP}$ cells in meninges and CNS parenchyma. **c**, Amounts of IFNγ and IL-17 (quantitative PCR) in T$_{MBP}$ cells from blood or the indicated CNS compartments at the indicated time points after transfer. Data are mean ± s.d. of duplicate measurements. Representative data of 4 independent experiments including at least 2 animals per group per time point. n.d., not determined owing to lack of cells within the CNS parenchyma at the early leptomeningeal T$_{MBP}$ cell infiltration phase. **d**, Cell surface expression of activation markers CD25 and CD134 (flow cytometry) of T$_{MBP–GFP}$ cells at day 4 after transfer. Black, isotype control; red, CD25 or CD134. Representative data of 4 independent experiments each combining cells from 4 or 5 animals for each compartment. **e**, Intracellular IFNγ and IL-17 production in T$_{MBP}$ cells isolated during the indicated phases of EAE. Representative data of 4 independent experiments each combining cells from 4 or 5 animals for each compartment ($n = 17$). **f**, CSF-derived T$_{MBP}$ cells produce cytokines upon antigenic stimulation in CSF. T$_{MBP–GFP}$ cells isolated at day 3 after transfer from CSF or cultured resting T$_{MBP–GFP}$ cells were stimulated *in vitro* with MBP in CSF from naive rats. IFNγ and IL-17 production (quantitative PCR). Data are mean ± s.d. of duplicate measurements representative of 2 independent experiments ($n = 8$). House-keeping gene, β-actin (*Actb*) (**c, f**).

a

Sorted T_MOG-GFP cells

b

T_MBP-GFP (green) T_MOG-GFP (green)

T_OVA-Cherry (red) T_MBP-GFP (green)/T_OVA-Cherry (red)

c

Meninges (total tissue)

Parenchyma (total tissue)

d

Sorted T cells

e

CSF Meninges Parenchyma

Extended Data Figure 5 | See next page for figure caption.

Extended Data Figure 5 | The trafficking of effector T cells in the CNS compartments depends on their reactivation levels and the inflammatory state in the CNS. a, T_{MOG} cells have a low encephalitogenic potential and display low reactivation levels in the CNS. Left, IL-17 and IFNγ expression measured by quantitative PCR in $T_{MOG-GFP}$ cells. House-keeping gene, β-actin (*Actb*) (**a, c, d**). Representative data of 3 independent experiments (data are mean ± s.d. of duplicate measurements). Note, T_{MOG} cells in meninges and CNS parenchyma produce less cytokines than the highly pathogenic T_{MBP} cells (Extended Data Fig. 4c), but more than non-pathogenic T_{OVA} cells (Extended Data Fig. 4d). Right, clinical course after $T_{MOG-GFP}$ cell i.v. transfer. Cumulative data of 3 independent experiments including at least 4 animals per group. T_{MOG} cell CNS infiltration in this model considerably precedes disease onset (Fig. 2e). **b,** Morphological analysis of the distribution of effector T cells with different antigen specificities and reactivation/pathogenic potentials in the CNS. Fluorescence-microscopy-derived overviews and magnified subsets (I–IV) of thoracic spinal cord sections showing distribution of fluorescently labelled T cells with the indicated antigen specificity 4 days after T-cell transfer. Open white and closed yellow arrows, representative T cells located in the meningeal compartment or in the CNS parenchyma, respectively. Scale bars: overviews, 200 μm; magnification, 100 μm.
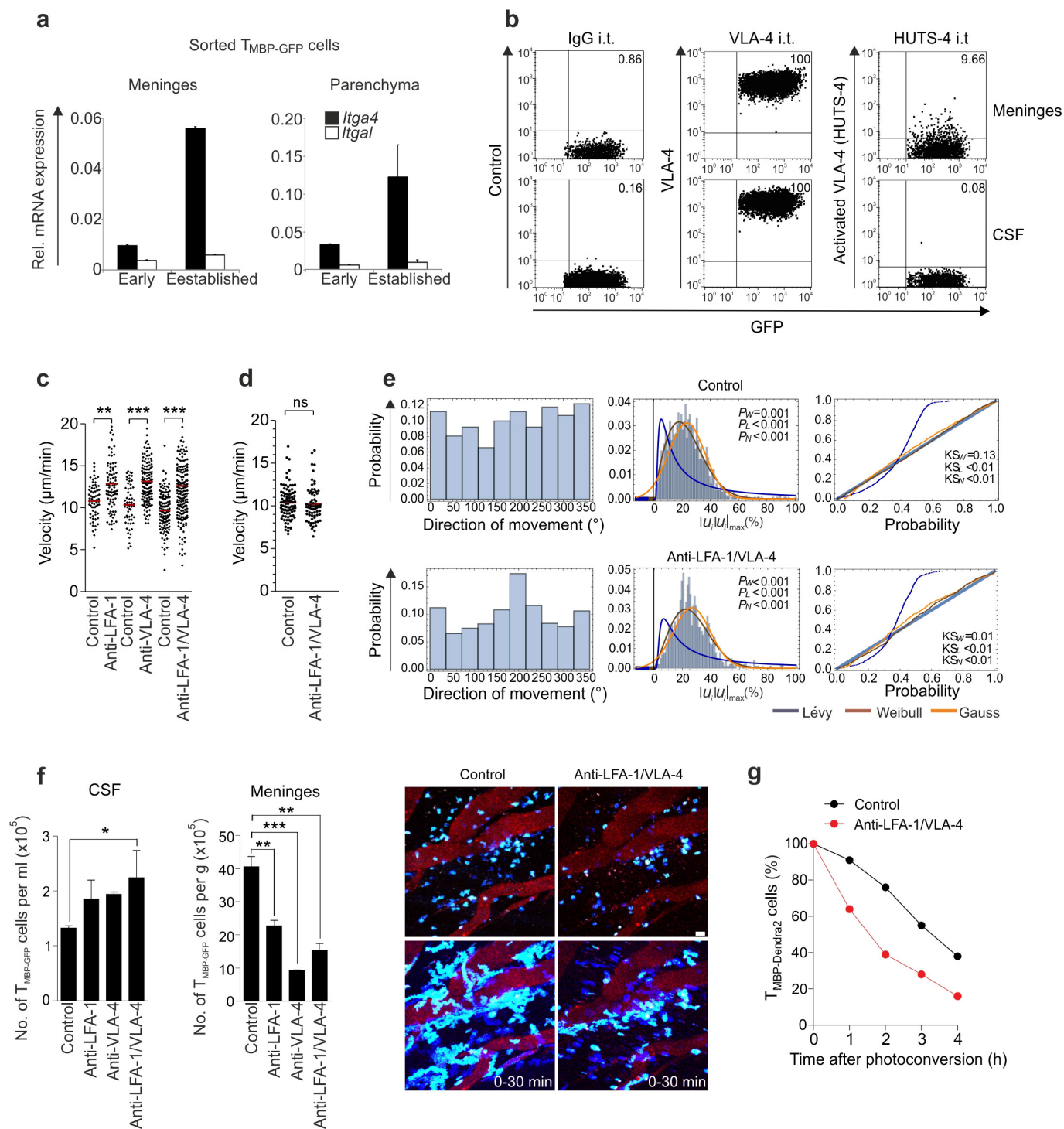
The infiltration behaviour of brain-non-reactive T_{OVA} cells is similar to that of pathogenic T_{MBP} cells when the CNS tissue is inflamed (after co-transfer of the T_{OVA} cells with T_{MBP} cells). **c,** T_{OVA} cells encounter an inflammatory milieu in the meninges when co-transferred with T_{MBP} cells. Quantitative PCR for the indicated chemokines, integrin ligands and cytokines was performed on meninges and CNS parenchyma isolated from naive animals (white columns) or from animals that 4 days previously had received either $T_{OVA-Cherry}$ cells (grey columns) or $T_{OVA-Cherry}$ cells together with $T_{MBP-GFP}$ cells (black columns). **d,** When co-transferred with T_{MBP} cells, T_{OVA} cells do not show signs of activation in the CNS. IFNγ and IL-17 expression (quantitative PCR) in $T_{MBP-GFP}$ or $T_{OVA-Cherry}$ cells sorted from the indicated compartments in animals transferred 4 days previously with these cells. Representative data of 3 independent experiments; data are mean ± s.d. of duplicate measurements (**c, d**). **e,** T_{OVA} cells are released from the meningeal compartment into the CSF in higher numbers than T_{MBP} cells. Quantification of $T_{OVA-Cherry}$ cells and co-injected $T_{MBP-GFP}$ cells during established leptomeningeal T_{MBP} cell infiltration (flow cytometry). Representative data of 3 independent experiments including 3 animals per group. Data are mean ± s.e.m. (two-tailed Mann–Whitney *U*-test).

Extended Data Figure 6 | See next page for figure caption.

Extended Data Figure 6 | T$_{MBP}$ cells in the leptomeningeal milieu closely interact with resident macrophages. a, Composition of the leptomeningeal milieu and interactions of T$_{MBP}$ cells with resident macrophages. Upper left, representative still and time-encoded projection illustrating, via a time colour-code scale, the area that single leptomeningeal macrophages scan with their processes over a recording period of 10 min (32 s time intervals). Green, GFP$^+$ meningeal macrophages in GFP$^+$ bone marrow chimaeras[7]; red, blood vessels. Upper right, original TPLSM picture and surface-rendered 3D reconstructions of a representative spot within the meningeal milieu during established leptomeningeal T$_{MBP}$ cell infiltration. Green, extravasated motile T$_{MBP-GFP}$ cells; red, meningeal phagocytes (MΦ); yellow trajectories, migration paths of individual T$_{MBP-GFP}$ cells; blue, collagen fibres. Magnification of an individual region (white dotted rectangle) indicates contacts (yellow arrows) between T$_{MBP-GFP}$ cells and meningeal phagocytes. Lower left, T$_{MBP}$ cells in direct contact (yellow) or not in contact (green) with meningeal macrophages (red). Surface-rendered 3D reconstruction of a representative still from a 30 min TPLSM recording. Lower right, a representative T$_{MBP-GFP}$ effector cell (red, false colour) migrating within the leptomeningeal compartment contacting several resident meningeal macrophages (1–5, yellow contours). Orange line, migration path of the T cell; green, T$_{MBP-GFP}$ cells; grey, vessel lumen (false colour). Scale bars, 50 μm. **b**, Ultrastructural analysis confirms direct and intense contacts between T cells and meningeal macrophages. Representative overview of cells within the spinal cord leptomeninges illustrating the organization of the leptomeningeal milieu at the ultrastructural level. Lymphocytes (L) in the subarachnoidal space are located between or adjacent to collagen fibrils (arrow heads) and in direct vicinity of phagocytes (MΦ) or local resident cells (M). Right, higher magnification of a lymphocyte in close contact with a macrophage. **c**, T$_{MBP}$ cells do not follow chemotactic gradients towards meningeal phagocytes. Vector analysis of the migration steps of T$_{MBP-GFP}$ cells in relation to a fixed macrophage in areas with a radius (ρ) of 25, 50 or 100 μm. The cosine of the angle between the macrophage–T-cell axes (AC) and the migration vector (AB) was calculated for each step. The values 1 or −1 correspond to a T$_{MBP-GFP}$ cell moving towards the meningeal phagocyte or in the opposite direction, respectively. Numbers indicate average direction ± s.d. of the steps examined for each radius. The average is always close to zero and the standard deviation is very broad, excluding the presence of targeted migration. Representative data of 4 independent experiments for each radius including 4396, 15870 and 57535 steps for $\rho = 25$, $\rho = 50$ and $\rho = 100$ μm, respectively. **d**, Integrin ligands are highly expressed in meningeal phagocytes. Bar plots show quantitative PCR data for the indicated integrin ligands on meningeal phagocytes labelled with Texas Red sorted from naive animals or during the early or established phases of leptomeningeal T$_{MBP}$ cell infiltration. House-keeping gene, β-actin (*Actb*). Mean ± s.d. of duplicate measurements. Histogram plots show corresponding protein expression (flow cytometry) during the established phase of leptomeningeal T$_{MBP}$ cell infiltration. Bottom, representative confocal images of leptomeningeal spots acquired in naive GFP$^+$ animals or in GFP$^+$ animals with established leptomeningeal T$_{MBP}$ cell infiltration after *in vivo* staining with the indicated antibodies. Single fluorescent channels and merged pictures. The expression of the tested integrin ligands is enriched in the vicinity of the leptomeningeal blood vessels in naive tissue (left) but widely distributed during the established phase of leptomeningeal T$_{MBP}$ cell infiltration (right).
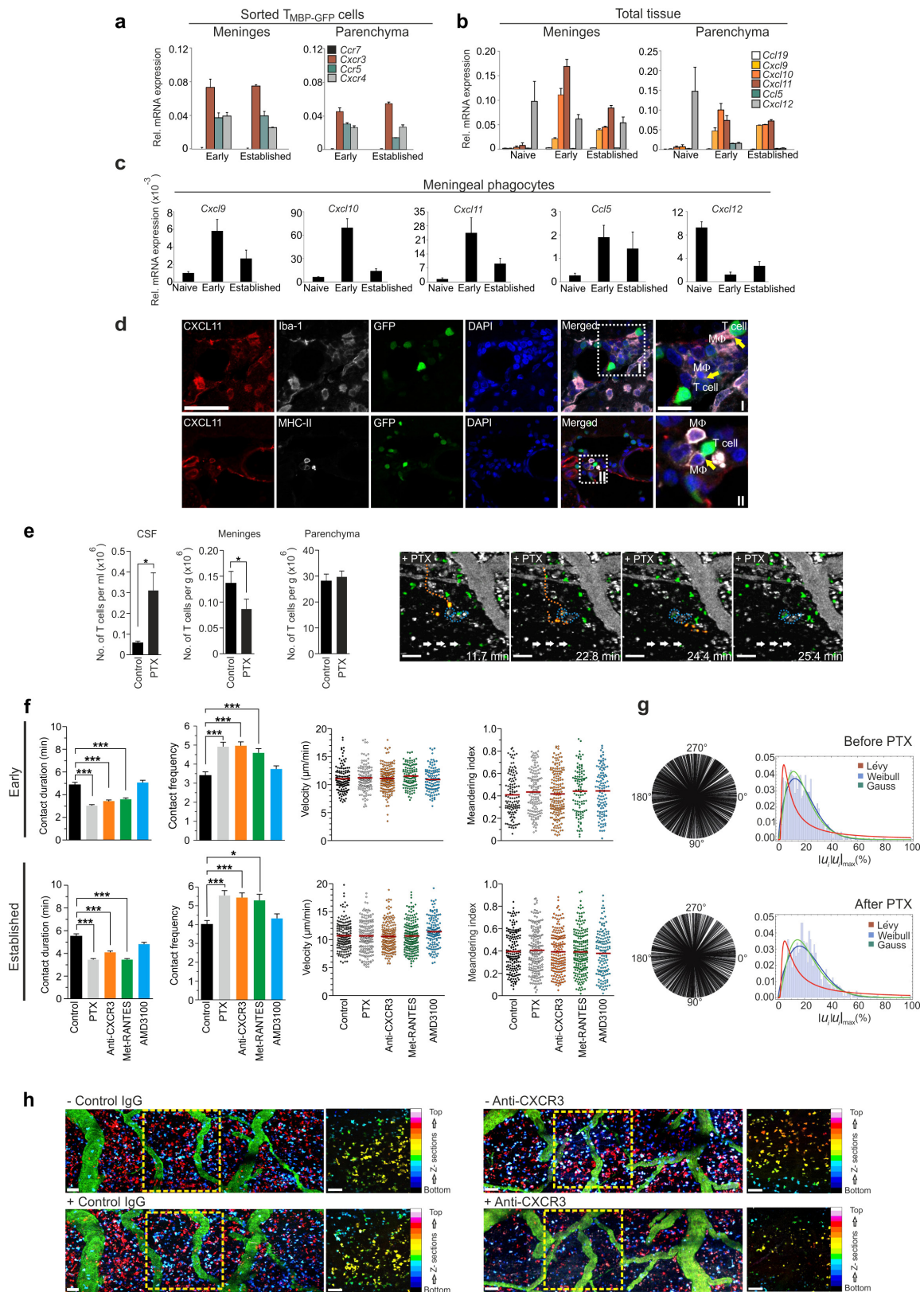
Extended Data Figure 7 | See next page for figure caption.

Extended Data Figure 7 | Locomotion behaviour of T_{MBP} cells in the leptomeningeal milieu and its regulation by VLA-4/LFA-1 integrins. **a**, T_{MBP} cells express high level of integrins. VLA-4 (*Itga4*) and LFA-1 (*Itgal*) expression (quantitative PCR) on $T_{MBP-GFP}$ cells from meninges or CNS parenchyma at the indicated time points of leptomeningeal T-cell infiltration. Representative data of 3 independent experiments. Data are mean ± s.d. **b**, VLA-4 is expressed in the active conformation on T_{MBP} cells in the leptomeninges but not in the CSF. HUTS-4 antibody (directed against the activated conformation of β1-integrins), activation-independent anti-VLA-4 antibody or control antibody were injected i.t. into Lewis rats during the established phase of leptomeningeal T-cell infiltration. $T_{MBP-GFP}$ cells were isolated from meninges and CSF 4 h later; protein expression was measured by flow cytometry. Percentages of positive T cells are indicated. Representative data of 3 independent experiments. **c**, Integrin blockade accelerates T-cell migration. Dot plots show $T_{MBP-GFP}$ cell velocity before (control) and 4 h after i.t. treatment with the indicated anti-integrin monoclonal antibodies. Data from 30 min TPLSM recordings on leptomeninges during the early phase of T_{MBP} cell leptomeningeal infiltration. Data are mean values of individual T cells from at least 3 independent experiments including 674 cells (Kruskal–Wallis ANOVA followed by Dunn's multiple comparison). **d**, T_{MBP} cell velocity is not influenced by integrins in the absence of CSF flow. Velocities of $T_{MBP-GFP}$ cells in the leptomeningeal milieu analysed during the established phase of leptomeningeal T_{MBP} cell infiltration after interruption of the CSF flow in the presence or absence (control) of anti-integrin monoclonal antibodies. The interruption of the CSF flow was achieved by removal of the arachnoidea causing the efflux of the CSF
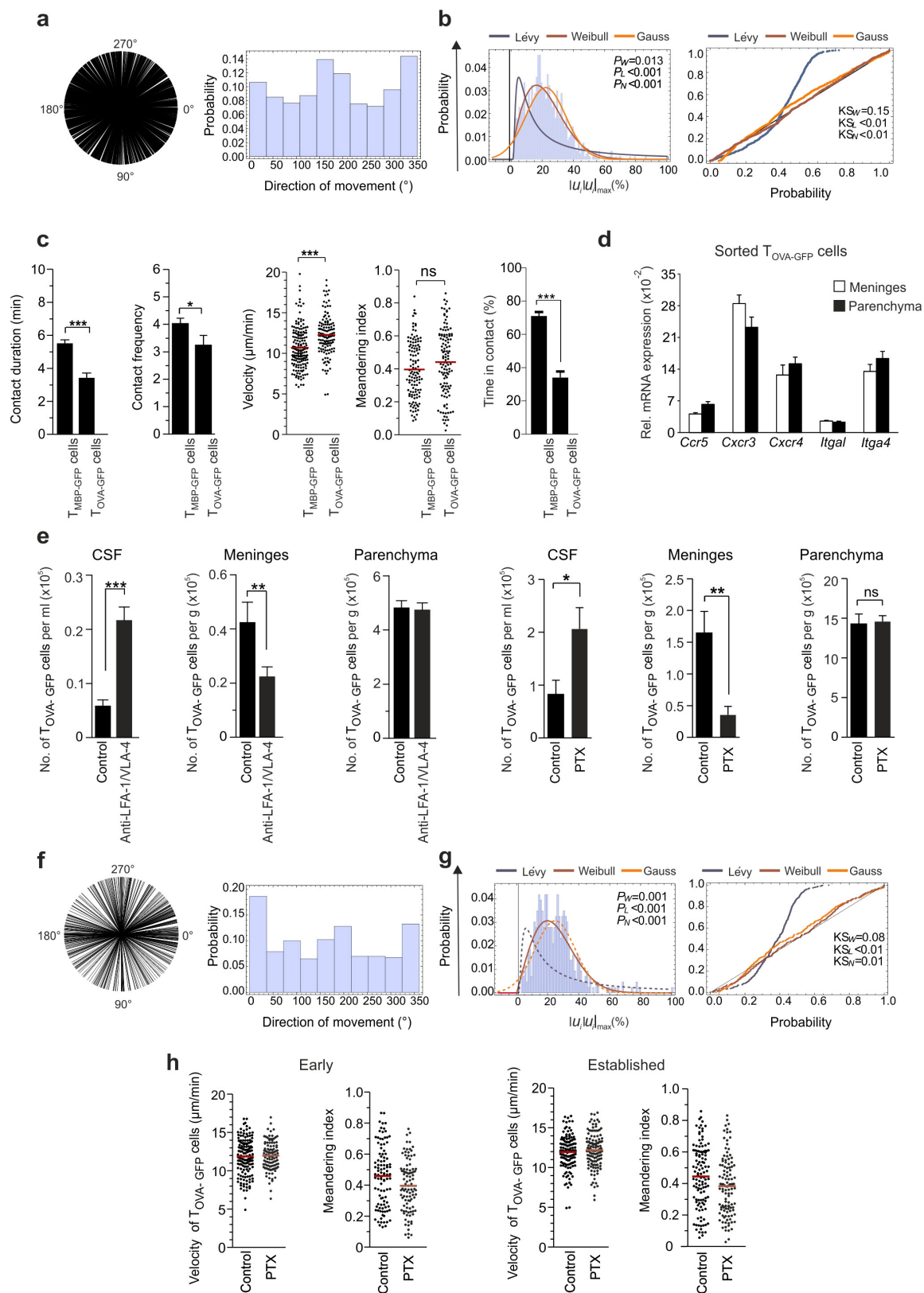
from the subarachnoidal space. 30 min TPLSM recordings. Data are mean values of individual T cells from 3 independent experiments including 166 cells (two-tailed Mann–Whitney *U*-test). **e**, Integrin blockade does not change the motility pattern of T_{MBP} cells. Mathematical analyses of at least 10 TPLSM recordings for each treatment (as in Fig. 3a, b). The Brownian walk of effector $T_{MBP-GFP}$ cells was not changed after i.t. application of anti-LFA-1/VLA-4 monoclonal antibodies. **f**, Effects of integrins on T_{MBP} cell adhesion to the leptomeninges during the early phase of meningeal infiltration resemble those during the established phase. 30 min intravital TPLSM recordings on leptomeninges during the early phase of leptomeningeal T_{MBP} cell infiltration. Animals were treated i.t. with PBS (control) or with the indicated anti-integrin monoclonal antibodies. Bar plots show number of $T_{MBP-GFP}$ cells 4 h after treatment in CSF and meninges (flow cytometry). At this time point no $T_{MBP-GFP}$ cells were detectable in the CNS parenchyma (Kruskal–Wallis ANOVA followed by Dunn's multiple comparison test). Images show representative stills from 30 min TPLSM recordings and corresponding time projections of T-cell tracks before and 4 h after the indicated treatment. T-cell detachment is indicated by the reduction of T_{MBP} cell trajectories after i.t. monoclonal antibody treatment. Blue, $T_{MBP-Lifeact-Turquoise2}$ cells. Scale bar, 50 μm. Representative data of 2 independent experiments. **g**, Integrin blockade increases the turnover of T_{MBP} cells in the leptomeninges. Quantification of photoconverted $T_{MBP-Dendra2}$ cells after i.t. application of anti-LFA-1/VLA-4 monoclonal antibodies or control IgG (control) during TPLSM of the established phase of leptomeningeal $T_{MBP-Dendra2}$ cell infiltration. Representative kinetic of at least 3 independent experiments. $*P < 0.05$, $**P < 0.01$, $***P < 0.001$ (**c**, **f**).

Extended Data Figure 8 | See next page for figure caption.

Extended Data Figure 8 | Role of chemokines in T$_{MBP}$ cell motility in the leptomeningeal milieu. a, Chemokine receptor expression profile of T$_{MBP}$ cells during EAE. Quantitative PCR data for the indicated chemokine receptors from T$_{MBP–GFP}$ cells isolated from spinal cord meninges and parenchyma during the early and established phases of leptomeningeal T$_{MBP}$ cell infiltration. Representative data of 3 independent experiments. Data are mean ± s.d. of replicate measurements. **b, c**, Inflammatory chemokines are upregulated in the CNS milieus and in meningeal macrophages during EAE. Quantitative PCR in naive animals or in animals during the early and established phases of leptomeningeal T$_{MBP}$ cell infiltration. Chemokine ligand expression either on meninges and CNS parenchyma (**b**) or on Texas-Red-labelled meningeal phagocytes isolated by flow cytometry (**c**). House-keeping gene, β-actin (*Actb*) (**a–c**). Representative data of 3 different experiments. Data are mean ± s.d. **d**, T$_{MBP}$ cells establish direct contact with CXCL11$^+$, MHC-II$^+$ meningeal phagocytes. Leptomeninges during early leptomeningeal T$_{MBP}$ cell infiltration stained for CXCL11, Iba-1 and DAPI (upper row) or CXCL11, MHC-II and DAPI (lower row). Green, T$_{MBP–GFP}$ cells. Scale bars, 50 μm. In the magnifications (right) yellow arrows indicate direct contacts between T$_{MBP–GFP}$ cells and CXCL11$^+$ meningeal phagocytes. Scale bars, 20 μm. **e**, Gα$_i$ signalling blockade induces a release of T$_{MBP}$ cells from the leptomeninges into the CSF. Left, plots show flow cytometry quantification of T$_{MBP–GFP}$ cells during established leptomeningeal T$_{MBP}$ cell infiltration in the indicated compartments 4 h after i.t. treatment with PBS (control) or PTX. Right, intravital image of spinal cord leptomeninges recorded 4 h after i.t. injection of PTX during the established phase of leptomeningeal T$_{MBP}$ cell infiltration. During the recording time, two T$_{MBP–GFP}$ cells highlighted in orange were released into the CSF. Grey (false colour), leptomeningeal blood vessels, phagocytes; green, T$_{MBP–GFP}$ cells; orange dotted lines, tracks of individual T$_{MBP–GFP}$ cells before being washed away into the CSF; blue dotted lines, contour of individual resident phagocytes; white arrows, direction of CSF flow. Scale bars, 50 μm. **f**, Interference

with chemokine signalling affects T$_{MBP}$ cell contacts with leptomeningeal phagocytes but not T$_{MBP}$ cell velocity and meandering index. 30 min time-lapse recordings during the early (upper plots) and established phases (lower plots) of leptomeningeal T$_{MBP}$ cell infiltration. Bar plots show mean contact duration and contact frequencies (early and established phases: 968 and 498 motile cells, respectively) between T$_{MBP–GFP}$ cells and Texas-Red-labelled meningeal phagocytes before (control) and 4 h after the indicated i.t. treatments. Data are mean ± s.e.m. of 3 independent experiments. Dot plots show T$_{MBP–GFP}$ cell velocity and meandering index before (control) and 4 h after the indicated i.t. treatment. Data are mean values of individual T cells from at least 3 independent experiments per treatment and time point (early phase 1506 cells and established phase 860 cells; Kruskal–Wallis ANOVA followed by Dunn's multiple comparison test). **g**, Gα$_i$ blockade does not change the migratory pattern of T$_{MBP}$ cells. Motility pattern of T$_{MBP–GFP}$ cells in the leptomeninges during the established phase of leptomeningeal T$_{MBP}$ cell infiltration before and 4 h after PTX treatment (as in Fig. 3a,b). Directional analysis and probability plots of T cell displacement for the Lévy (red), Weibull (blue) and normal (Gauss, green) distributions. The T$_{MBP–GFP}$ cells maintained their Brownian walk after PTX treatment. Analysis of at least eight TPLSM recordings. **h**, CXCR3 blockade alone recapitulates the effect of Gα$_i$ inhibition on T$_{MBP–GFP}$ cells released from the meninges into the CSF. Representative TPLSM overviews of spinal cord leptomeninges before and 8 h after i.v. injection of isotype control antibodies (control IgG) or anti-CXCR3 monoclonal antibody during established leptomeningeal T$_{MBP}$ cell infiltration. Magnification of individual regions originating from the overviews illustrate the position of the effector T cells in the *z*-axis in the leptomeningeal space via a colour-code scale. Note, T$_{MBP–GFP}$ cells are preferentially detached from the surface of the pia mater. Green, leptomeningeal blood vessels; red, phagocytes; blue, T$_{MBP–Lifeact–Turquoise2}$ cells. Scale bars, 50 μm. *$P < 0.05$, ***$P < 0.001$ (**e, f**).
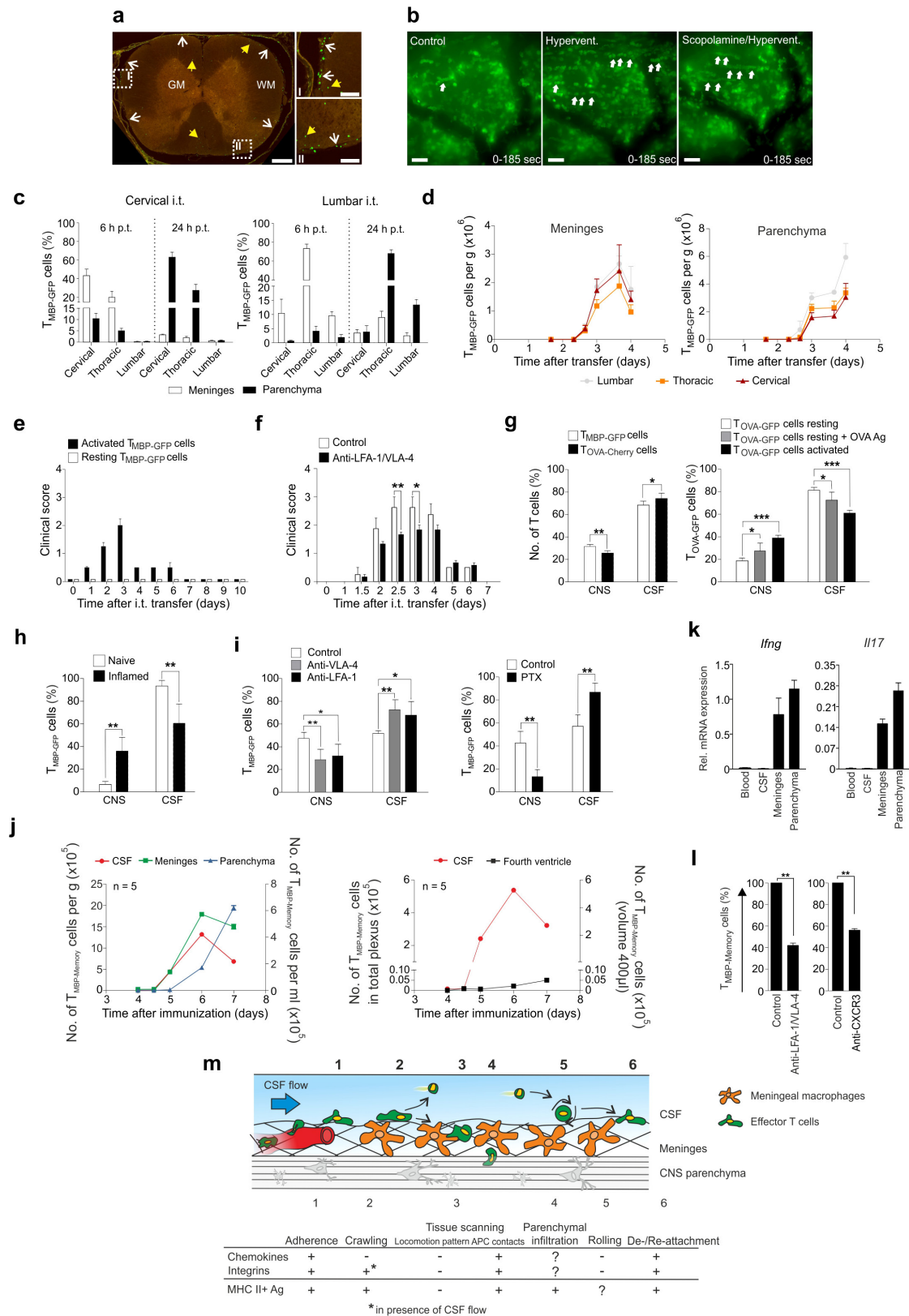
Extended Data Figure 9 | See next page for figure caption.

Extended Data Figure 9 | Motility pattern of brain-non-reactive T_{OVA} cells in the leptomeninges and their detachment into the CSF.
a, b, The motility pattern of T_{OVA} cells in the leptomeninges resembles that of T_{MBP} cells. $T_{OVA–GFP}$ cell motility in the leptomeninges during established inflammation (TPLSM 3.5 days after co-transfer with non-labelled T_{MBP} cells). **a**, T_{OVA} cells do not follow a preferential direction. Directional analyses of the $T_{OVA–GFP}$ cell tracks (as in Fig. 3a). Directions of in-plane movement (left) and associated probability for an angle varying within [0; 360] degrees in the fitting plane (right). **b**, T_{OVA} cells move in a Brownian random walk. Motility pattern of $T_{OVA–GFP}$ cells (as in Fig. 3b). Analysis of at least 6 TPLSM recordings. **c**, $T_{OVA–GFP}$ cells are less adhesive to meningeal structures in comparison to their myelin-reactive counterparts. Mean contact duration (417 contacts per 127 cells); contact frequencies (127 cells) between MBP- or OVA-reactive T cells and meningeal phagocytes; mean velocities (304 cells) and meandering indices (236 cells) of MBP- or OVA-reactive T cells; percentage of time spent by these T cells in contact with meningeal phagocytes during the 30 min recording. Results from intravital TPLSM recordings during established meningeal inflammation on spinal cord leptomeninges, after transfer of $T_{MBP–GFP}$ cells or of $T_{OVA–GFP}$ cells together with non-labelled T_{MBP} cells. Data are mean values ± s.e.m. of 3 independent experiments per transfer (two-tailed Mann–Whitney U-test). **d**, Chemokine receptors and integrin expression in $T_{OVA–GFP}$ cells. $T_{OVA–GFP}$ cells transferred into Lewis rats together with non-labelled T_{MBP} cells were sorted from meninges and CNS parenchyma during established meningeal inflammation. Quantitative PCR. House-keeping gene, β-actin (*Actb*). Representative data of 3 independent experiments. Data are mean ± s.d. of duplicate measurements. **e**, Integrin or Gα$_i$ signalling interference induces a release of $T_{OVA–GFP}$ cells from the leptomeninges into the CSF. $T_{OVA–GFP}$ cells were co-injected with non-labelled T_{MBP} cells. During established meningeal inflammation (3.5 days after transfer) animals were treated i.t. with PBS (control), anti-LFA-1/VLA-4 monoclonal antibodies (left) or PTX (right). Absolute numbers of $T_{OVA–GFP}$ cells in CSF, spinal cord meninges and parenchyma 4 h after treatment. Data are mean ± s.e.m. of representative data from at least 3 independent experiments per treatment including 3 animals per group (two-tailed Mann–Whitney U-test). **f–h**, Gα$_i$ signalling interference does not change the motility pattern of T_{OVA} cells. **f, g**, The Brownian walk of T_{OVA} cells was not changed after PTX treatment. Directional analyses and motility pattern of $T_{OVA–GFP}$ cells 4 h after i.t. injection of PTX. Mathematical analyses of at least 6 TPLSM recordings (as in Fig. 3a, b) 4 days after co-transfer with T_{MBP} cells. **h**, Interference with chemokine signalling does not affect T_{OVA} cell straightness and velocity. Mean velocities (498 cells) and meandering indices (428 cells) of $T_{OVA–GFP}$ cells at the depicted time points of leptomeningeal T-cell inflammation. 30 min TPLSM recordings were acquired before and 4 h after i.t. treatment with PTX. *$P < 0.05$, **$P < 0.01$, ***$P < 0.001$ (**c–e**).

Extended Data Figure 10 | See next page for figure caption.

Extended Data Figure 10 | Reattachment of T$_{MBP}$ cells from the CSF to the leptomeninges and its regulation by integrins, chemokines and T-cell activation/CNS inflammation. a, Distribution of reattached T$_{MBP}$ cells resembles that of early EAE lesions. T$_{MBP-GFP}$ cells are located diffusely in the meninges and the adjacent spinal cord parenchyma after reattachment from the CSF. T$_{MBP-GFP}$ cells retrieved from CNS tissue on day 3 after transfer were injected i.t. into naive animals. Fluorescence microscopy images of the fixed cervical spinal cord 20 h later. Insets, magnifications of areas of interest (right; I, II). Arrows, T$_{MBP-GFP}$ cells in the leptomeninges (white) and CNS parenchyma (yellow). Green, T$_{MBP-GFP}$ cells. Scale bars, 100 μm. **b**, Increased T$_{MBP}$ cell rolling and floating after forced ventilation indicate that respiration is a major driving force for the spinal cord CSF flow. Time-lapse video microscopy of T$_{MBP-GFP}$ cells during the established phase of leptomeningeal T$_{MBP}$ cell infiltration performed under 3 different conditions: (1) during standard conditions (control; respiration rate: 81 bpm; cardiac rate: 230 bpm); (2) during hyperventilation (hypervent; respiration rate: 100 bpm; cardiac rate: 200 bpm); and (3) during hyperventilation following administration of methylscopolamine (0.05 mg kg^{-1}) to block the hyperventilation-induced vagal influence on the heart (Scopolamine/hypervent; respiration rate: 100 bpm; cardiac rate: 230 bpm). Hyperventilation induced a strong increase in rolling/floating T$_{MBP-GFP}$ cells that was not changed after methylscopolamine. 185 s time projections. Green, T$_{MBP-GFP}$ cells; white arrows, representative T cells rolling/floating in the CSF. Scale bars, 50 μm. Representative data of 3 independent experiments. **c**, T$_{MBP}$ cell transport in the CSF after i.t. injection. Distribution of T$_{MBP-GFP}$ cells in different levels of the spinal cord tissues after localized injection of the cells into the cisterna magna or the subarachnoidal space of the lumbar spinal cord. Flow cytometry analyses. Relative numbers of T$_{MBP-GFP}$ cells 6 and 24 h after i.t. transfer in the indicated CNS compartments. Combined results of 2 independent experiments for each i.t. injected site ($n = 14$). **d**, T$_{MBP}$ cell infiltration in the different levels of the spinal cord during transfer EAE. Quantification (flow cytometry) of T$_{MBP-GFP}$ cells in the meninges or parenchyma of the indicated parts of the spinal cord. Data are mean ± s.e.m. of representative data from 2 independent experiments per treatment including 2 or 3 animals per group ($n = 41$). **e**, Activated but not resting T$_{MBP}$ cells induce EAE after i.t. transfer. T$_{MBP-GFP}$ cells activated by antigenic stimulation or resting cells were i.t. transferred into naive animals. Clinical scores at the indicated time points. Representative results of 3 independent experiments with 4–6 animals per group. Data are mean ± s.d. ($n = 28$). **f**, Interference with integrin binding reduces the encephalitogenic potential of i.t. transferred T$_{MBP-GFP}$ cells. T$_{MBP-GFP}$ cell blasts were pre-treated with either an IgG control antibody or a combination of anti-LFA-1/VLA-4 monoclonal antibodies before i.t. transfer into naive animals. Clinical scores. Representative results of 3 independent experiments with 2 or 3 animals per group. Data are mean ± s.e.m. ($n = 16$, two-tailed Mann–Whitney U-test). **g**, T$_{MBP}$ cells invade the inflamed CNS tissue more efficiently than T$_{OVA}$ cells. Left, the same number of non-activated T$_{MBP-GFP}$ and T$_{OVA-Cherry}$ cells were co-injected i.t. into animals at the onset of clinical EAE, that is, 3 days after i.v. transfer with unlabelled T$_{MBP-GFP}$ cells. 20 h after i.t. injection, the entry of T$_{MBP-GFP}$ and T$_{OVA-Cherry}$ cells into the CNS tissue

(including spinal cord meninges and parenchyma) was quantified by flow cytometry. Representative results of 2 independent experiments with 4 animals per group. Data are mean ± s.d. ($n = 8$). Right, resting or *in vitro* activated T$_{OVA-GFP}$ cells were i.t. injected into naive animals. In addition, a group of animals receiving resting T$_{OVA-GFP}$ cells were co-injected intrathecally with 25 μg of OVA antigen. 20 h after i.t. injection, T$_{OVA-GFP}$ cells in the spinal cord tissue were quantified. Representative of 2 independent experiments with 2 animals per group. Data are mean ± s.d. ($n = 12$, two-tailed Mann–Whitney U-test (left) or Kruskal–Wallis ANOVA followed by Dunn's multiple comparison test (right)). **h**, Inflammation of the CNS tissue increases T$_{MBP}$ cell entry from the CSF. CSF-derived T$_{MBP-GFP}$ cells were injected i.t. either into naive animals or into animals at the onset of clinical EAE, that is, 3 days after i.v. transfer of non-labelled T$_{MBP}$ cells (that is, inflamed condition). Cell quantifications of T$_{MBP-GFP}$ cells in the CNS tissue and CSF by flow cytometry 20 h later when the re-transferred T cells had maximally infiltrated the inflamed CNS of the recipient animals. Data are mean ± s.d. of representative results of 3 independent experiments ($n = 12$, two-tailed Mann–Whitney U-test). **i**, Blocking of integrin or Gα$_i$-signalling reduces T$_{MBP}$ cell migration from the CSF into the inflamed CNS tissue. CNS-derived T$_{MBP-GFP}$ cells were pre-treated with anti-VLA-4 or anti-LFA-1 monoclonal antibodies or with isotype control IgG antibody (control) (left) or PTX or PBS as control (right). Cells were then injected i.t. in animals at the onset of EAE and quantified as in **h**. Data are mean ± s.d. of representative results of 3 independent experiments ($n = 18$, Kruskal–Wallis ANOVA followed by Dunn's multiple comparison test (left) or two-tailed Mann–Whitney U-test, right)). **j–l**, In active EAE induced by reactivated memory T$_{MBP}$ cells , trafficking of the memory T$_{MBP}$ cells between the distinct CNS compartments follows the same rules as the trafficking of T$_{MBP}$ cells during transfer EAE. **j**, Memory T$_{MBP}$ cells accumulate simultaneously in the meninges and the CSF before they occur in the choroid plexus. Quantification (flow cytometry) of GFP$^+$ T$_{MBP-Memory}$ cells in CSF, spinal cord meninges and parenchyma (left), or in CSF and choroid plexus of the fourth ventricle (right) at the indicated time points after immunization of 10-week-old memory animals. Data are mean ± s.d. of 3 independent experiments ($n = 13$). **k**, CSF-derived memory T$_{MBP}$ cells present a low activation profile. IFNγ and IL-17 expression (quantitative PCR) in GFP$^+$ memory T$_{MBP}$ cells 5 days after immunization. House-keeping gene, β-actin (*Actb*). Representative data of 3 independent experiments. Data are mean ± s.d. of duplicate measurements. **l**, Integrin and chemokine blockade reduces the number of T$_{MBP-Memory}$ cells in the leptomeninges during active EAE. Intravital TPLSM recordings of spinal cord leptomeninges from 10-week-old memory animals 5 days after immunization. Quantification of GFP$^+$ memory T$_{MBP}$ cells in the acquired images before (control) and 4 h after i.t. treatment of either anti-LFA-1/VLA-4 or anti-CXCR3 blocking monoclonal antibodies. Data are mean values ± s.e.m. from 3 independent experiments including 5,947 cells (two-tailed Mann–Whitney U-test). *$P < 0.05$, **$P < 0.01$, ***$P < 0.001$ (**g–i**, **l**). **m**, Schematic representation of the migratory behaviour of effector T cells in the leptomeningeal milieu and the roles of chemokines, integrins and activation in controlling the T-cell migration steps. Question marks indicate unresolved points.